Long-term ash dispersal dataset of the Sakurajima Taisho eruption for ashfall disaster countermeasure

Haris Rahadianto[1, 2], Hirokazu Tatano[2], Masato Iguchi[3], Hiroshi L. Tanaka[4], Tetsuya Takemi[2], Sudip Roy[5]

[1]Graduate School of Informatics, Kyoto University, Kyoto, 606-8501, Japan
[2]Disaster Prevention Research Institute, Kyoto University, Uji, 611-0011, Japan
[3]Sakurajima Volcano Research Center, Disaster Prevention Research Institute, Kyoto University, Sakurajima, 851-1419, Japan
[4]Center for Computational Sciences, Division of Global Environmental Science, University of Tsukuba, Ibaraki, 305-8577, Japan
[5]Department of Computer Science and Engineering, Indian Institute of Technology Roorkee, Roorkee, Uttarakhand, 247-667, India

Correspondence to: Haris Rahadianto (haris.rahadianto.88n@st.kyoto-u.ac.jp)

Abstract. A large volcanic eruption can generate large amounts of ash which can affect the socio-economic activities of surrounding areas. Eruption scale and weather conditions primarily contribute to escalate ashfall hazards to wider areas. Accumulated ashfall has devastating impacts on both surrounding areas of the volcano and other regions, affecting airline transportation, socio-economics activities, and human health. Therefore, it is crucial to discover places with a high probability of exposure to ashfall deposition. In this study, we present an ashfall deposit and airborne ash concentration dataset from an ash dispersal simulation of a large-scale explosive volcanic eruption as a reference for ashfall disaster countermeasures. We selected the Taisho (1914) eruption of the Sakurajima volcano, as our case study. This eruption regarded as the strongest eruption in Japan in the last century, and our study provides a baseline for the worst-case scenario. We employed one eruption scenario approach by replicating the actual eruption under various extended weather conditions to show how it would affect contemporary Japan. We generated an ash dispersal dataset by simulating the ash transport of the Taisho eruption scenario using a volcanic ash dispersal model and meteorological reanalysis data for 64 years (1958-2021). We explain the dataset production process and provide the dataset in multiple formats for broader audiences. We further clarified the validity of the dataset with its limitations and uncertainties. By having an extensive dataset on ash dispersal in wider areas for a worst-case scenario, comprehensive countermeasure strategies can be derived to further reduce ashfall risk. The dataset is available at the DesignSafe-CI Data Depot: https://www.designsafe-ci.org/data/browser/public/designsafe.storage.published/PRJ-2848v2 or through the DOI: https://www.doi.org/10.17603/ds2-vw5f-t920 by selecting Version 2 (Rahadianto and Tatano, 2020).

1 Introduction

A volcanic eruption is one of the events that emits several dangerous pollutants affecting human lives. Large eruptions eject enormous amounts of tephra and other eruptive materials into the air. Tephra hampers the residents near the volcano and citizens in the farther areas (Bonadonna et al., 2021) in the form of very fine ash. When a large eruption occurs, volcanic ash can travel far away from the volcano source, disrupting socio-economic activities in many different ways, for example, damaging critical infrastructures and buildings, and causing health problems among the people (Wilson et al., 2012; Zuccaro et al., 2013). Settled volcanic ashes (i.e., ashfall) are directly affects human health and livelihoods, destroying vegetation, crops, and pastures, causing physical damages to infrastructure, such as clogging drainage systems, contaminating water supplies, disrupting traffic, and damaging the vehicles on roads (Barsotti et al., 2010; Ayris and Delmelle, 2012; Damby et al., 2013; Zuccaro et al., 2013; Poulidis et al., 2018). The cumulative weight of ashfall on the roof can collapse buildings and cause short-circuit electricity inside them (Zuccaro et al., 2013; Hampton et al., 2015). In addition, ash plumes from the volcanoes are a safety hazard that can severely damage commercial airlines (Folch et al., 2012; Peng and Peterson, 2012; Tanaka and Iguchi, 2019). The 2010 eruption of Eyjafjallajökull has amplified the evidence. During this event, volcanic ashes flew to thousands of kilometres away, forcing almost all airports in 25 countries to close for a week-long and costing a loss of billions of dollars in revenue for airlines (Folch et al., 2012; Peng and Peterson, 2012). Apart from the eruption scale, the weather conditions, mainly winds, primarily contribute to escalating ashfall catastrophes to a broader range. Ashfall hazards are uncertain based on (1) the eruption magnitude and intensity and (2) the wind condition at the time of eruption that can bring ashes to distant places. Based on the evidence that ashfall hazards have dynamically changing exposures toward socio-economic activities, we believe that estimating the risk of finding effective countermeasures is critical.

Currently, densely populated and modernised cities require comprehensive volcanic risk reduction strategies (Miyaji et al., 2011). One of the necessary actions to lessen the impacts of ashfall hazards is assessing the risk to infrastructures, human lives, and economic impacts to develop a better response plan. Accordingly, the hazards and risk assessment for ashfall mostly relies on quantifying accumulated ashfall on the ground, then extending the analysis by combining social data, based on the interest (population data, building data, and many more). Many researchers have used this typical method to determine the expected impacts probability for future eruption events (Jenkins et al., 2014, 2015, 2018; Wilson et al., 2012; Biass et al., 2017). A comprehensive ashfall risk assessment requires both long-term weather and simulations for statistical analysis purposes, such as selecting typical conditions and analysing circumstances under exceptional conditions (Hattori et al., 2013, 2016). An important component of conducting such a study is to obtain long-term ashfall deposit data encompassing vast impact areas during an extended period. This paper presents the generated dataset of the ash dispersal products over a vast region over 64 years (1958-2021) to provide vital input for the development of a more comprehensive ashfall risk assessment and emergency management. Sakurajima volcano was selected as an area of interest because of its high explosivity and potential for large-scale explosive eruptions within the following 20–25 years (Yamasato et al., 2013; Hickey et al., 2016; Biass et al., 2017; Poulidis et al., 2018).

As supporting evidence, three large eruptions of Sakurajima volcano have occurred within the last six centuries: the Bunmei eruption in 1471, the An'ei eruption in 1779, and the Taisho eruption in 1914. The latter was considered the largest and the strongest eruption in Japan during the last century (Todde et al., 2017; Poulidis et al., 2018). Furthermore, Hickey et al. (2016) showed that similar phenomena of magma supply rates that led to the Taisho eruption are currently occurring, suggesting 130 years return period from the last eruption to the next one in the future. Consequently, the Sakurajima volcano tended to have another large-scale explosive eruption in the following multiple decades. To address such an urgent issue, the Kagoshima City municipal government has been preparing a risk management and evacuation plan by providing an updated Sakurajima volcano hazard map. The hazard map contains the necessary information about the impacts of historical eruptions, volcanic alerts and warnings, with guidelines on evacuation directions and procedures (Kagoshima City, 2010). Furthermore, the Osumi Office of the Rivers and National Highways produced maps for the potential ash deposition from a large eruption case in municipalities surrounding the Sakurajima volcano (Kyushu Regional Development Bureau, 2017). Recently, some studies have assessed the impacts of both continuous Vulcanian activities and scenarios for an explosive eruption of Sakurajima volcano, providing insights into how volcanic ashes could disperse and affect livelihoods (Biass et al., 2017; Poulidis et al., 2018). However, those studies and precautions only discussed the proximal impacts in short to medium terms, with no further analysis available for the impacts to the distal locations. Furthermore, the previous large-scale explosive eruptions have brought calamities across almost all of Japan. Thus, it is crucial to assess and develop a comprehensive risk analysis for a broader range, because when the ashfall arrives in major socio-economic centres of Japan, such as Fukuoka, Osaka, and Tokyo, a larger population will be exposed.

The primary aim of this study is to provide the necessary information, vital in modern times regarding ashfall disaster countermeasures. Using the Taisho eruption case, we simulated the volcanic ash transport and dispersion model (VATDM) to demonstrate an ash dispersal process in large areas (entire Japan). We approached this issue by adapting one eruption scenario (OES) strategy, specifically as a baseline for the worst-case scenario (Bonadonna, 2006; Barsotti et al., 2018). We conducted this simulation over an extended period (1958–2021, 64 years) with a long-term weather reanalysis data to compensate for the incomplete wind profiles at the time of the eruption and to further validate the dataset. Our study is an attempt to characterise ashfall impacts from the Taisho eruption to contemporary Japan and understand the variety of ash dispersal characteristics of a large-scale explosive eruption at Sakurajima volcano. Furthermore, it is important to recognise the behaviour of ash transport, starting from discovering the condition of reproducing the actual ashfall distribution to finding the condition that leads to much worse consequences. We produced this dataset for various purposes and usage, such as estimating the volcanic ashfall risk by analysing both the dispersal and deposition patterns of volcanic ashfall over a long period, developing the hazard maps for the disaster risk management process, and seeking a better comprehension of the tendency of ashfall distribution from a large eruption over an extensive region. Given the size of the dataset, the available information (ground deposits and airborne concentrations) will help users make response preparation, such as the creation of conditional ashfall risk maps, early warning system enhancement, planning for ash clean-up operations, closure management on both air and land transportation, and long-term long-distance evacuation.

This paper is structured as follows: Section 1, introduces the general background and motivation for this study, followed by Section 2, which presents the process and impacts of the ashfall dispersal from the Taisho eruption in 1914, derived from previous studies and historical reports of the eruption. Section 3 describes the methodology for producing the dataset, and Section 4 describes the format and the usage examples of the dataset. Section 5 thoroughly addresses the validation method with the limitations of the dataset. Finally, Section 6 concludes the paper. Unless otherwise specified, all time dimensions in this study use the Japan Standard Time (JST, +09UTC).

2 Ashfall dispersal during the Taisho eruption

The Taisho eruption was extensively studied by researchers all over the world, mainly due to:

1. Detailed historical reports in English were compiled and available shortly after the eruption (Omori, 1914; Koto, 1916).
2. The concurrent unrest activities of the Sakurajima volcano (Iguchi, 2016; Iguchi et al., 2020; Poulidis et al., 2017, 2018).
3. The high possibility of a large-scale explosive eruption in the next decades that probably would resembles the past event (Hickey et al., 2016).

This section focuses on how volcanic ashes travelled during the eruption process, especially to distal locations spread across Japan. For reference regarding to the complete evidence and chronology of the Taisho eruption, please refer to the chronicles mentioned above and the studies conducted by Kobayashi (1982); Yasui et al. (2006, 2007); and Todde et al. (2017). The explanation here refers to, unless specified otherwise, both historical chronicles and the latest comprehensive study by Todde et al. (2017). The Taisho eruption is a large-scale explosive eruption with a Volcanic Explosivity Index (Newhall and Self, 1982) (VEI) of 4. The Taisho eruption ejected an enormous volume of eruptive materials from the two main active vents during its explosive phases. The explosive eruption started at 12 January 1914 10:00:00 and lasted 48 h. The tephra mostly ejected from the western vent (Nabeyama) mixed with those from the eastern vent (Yokoyama), simultaneously producing plumes estimated to be between 10 km and 18 km high. The westerlies at the upper altitude and the surface winds influence the ashfall dispersal pattern. Both the prevailing winds and plume height were significant drivers of the vast ash deposition process over a very wide area. Most tephra dispersed eastward, leaving Kagoshima City with only minor ash deposits during the first several days of the eruption.

In contrast, the location close to the eastern vent had four meters deep ashfall deposit. Three days after the eruption started, the ashfall deposits were reported in Kyushu, Shikoku, western Japan, and Sendai in northern Japan. Village offices, tobacco plantations, and local meteorological observatories kept a record of the exact time of ash arrival and sighting, showing that volcanic ashes reached the major cities of Fukuoka at 08:00:00 and Osaka at midnight on 13 January 1914, Tokyo on the morning of 14 January 1914, and finally Sendai in the afternoon of the same day.

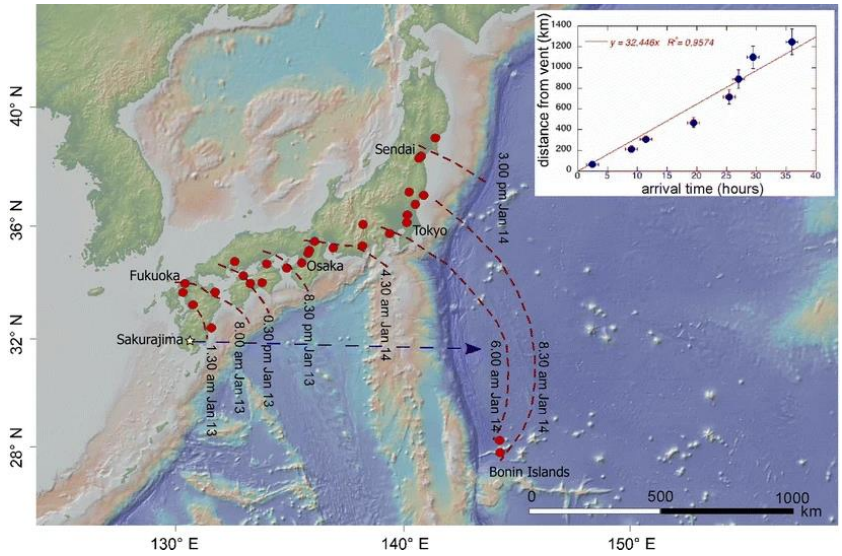

Figure 1. The arrival time of ashfall during the Taisho eruption event throughout Japan. The blue dashed line indicates the chronology of ash sighting in each respective location. Inset, the graph of ash observation time from the eruption source (Todde et al., 2017).

Another important notion is the report of heavy ash fallout (~1.5 × 10^6 km^2) at Ogasawara (Bonin Islands), approximately 1222 km away from the vent. Before reaching the climactic phase, the dispersal of very fine ashes during the first 13 h of eruption may have caused this phenomenon. Meanwhile, the activity of the eruption in the following days was largely minor in intensity, and ashfall continued to occur within the 200 km range from the volcano until 19 January 1914. Todde et al. (2017) presented a simple and straightforward isochrones map derived from the chronicles in Fig. 1. The previous study which produced this map reported that the average velocity of the winds carrying the tephra was found to be approximately 9 ms^{-1}. Unfortunately, although there is an abundance of ashfall reports across Japan, no concrete measurement of the extent of ash dispersal can be obtained. As most of the recent research has only focused on the proximal impacts near the volcano, there is still a lack of complete analysis of the effects in distal locations. Based on the collected reports, there was only one attempt found to completely draw all ashfall-affected areas. The wide exposure map, shown in Fig. 2, did not get the same interest in modernisation compared to the dispersal maps at proximal regions that have been recently updated (see supplementary materials by Todde et al., (2017) and the latest report conducted by Mita et al., (2018)). Those proximal ash dispersal maps showing the eruption impacts in the southern Kyushu region contains complete information regarding the ground measurement of ash deposits. However, the map of ash dispersal for all of Japan did not have exact ash measurements. The information provided in Fig. 2 is limited but vital, as the extent of the distance travelled by the ashfall is known. Fast-travelling ash endangers a larger population and significantly disrupts airline transportation. Evidence from the latest large eruption events (e.g., St. Helens in 1980, Pinatubo in 1991, Eyjafjallajökull in 2010) demonstrated the cataclysmic consequences of ashfall in wider areas (Tilling et al., 1990; Fero et al., 2008, 2009; Folch et al., 2012; Peng and Peterson, 2012).

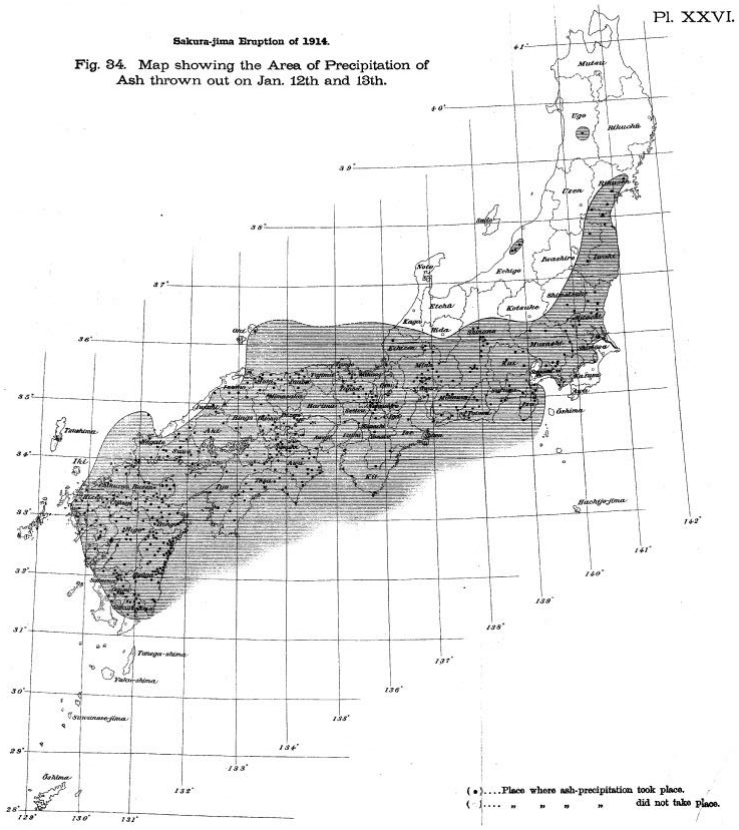

Figure 2. The ash dispersal map of the Taisho eruption on all of Japan (Omori, 1914).

Economic losses amounted to billions because obstructed air transportation was one of the more significant repercussions. These losses were not realised by the authorities during the Taisho eruption event that occurred more than a century ago. Moreover, the Japanese airspace would suffer worse implications if a similar explosive eruption occurred shortly. At least 40% of the air traffic in the Japanese airspace will be affected if Sakurajima volcano has a large-scale explosive eruption in the present day. The number of passengers affected was almost four times higher than the number of people affected by devastating Typhoon Jebi back in 2018 (Takebayashi et al., 2021). The currently built environment and infrastructures vulnerable to ashfall hazards require better comprehension of the upcoming volcanic risk for locations proximal as well as distal to the volcano. It is urgent to learn how large the catastrophe would affect contemporary Japan if the same event occurred in recent times.

3 Data generation methods

3.1 Simulation on selected eruption scenario

We used a fixed volcanological scenario over an extended contemporary period recorded in the meteorological reanalysis dataset to capture the extended daily variability of ash dispersal patterns from the Taisho eruption. We ran the PUFF model for cases of 23,376 days from 1 January 1958 to 31 December 2021.The PUFF model is an ash tracking model developed during the Redoubt volcano eruption in 1989, which is famous for its high resolution and high accuracy results (Tanaka, 1994; Searcy et al., 1998; Scollo et al., 2011; Folch, 2012). This model considers ash as a collection of a finite number of virtual particles, computes the motion of the particles over time, and works better within the first 48 hours of the eruption (Searcy et al., 1998; Tanaka, 1994). The PUFF model is a Lagrangian-based model that has several advantages compared to other approaches (Eulerian), such as providing trajectory information, physical realism, describing non-diffusive near-field to sources, numerical stability, lack of numerical diffusion, conservation properties, and resolution of sub-grid scale variability (Lin et al., 2012). Among all the nine Volcanic Ash Advisory Centers (VAACs) worldwide, eight VAACs, including Tokyo VAAC, use and operate models with the Lagrangian approach (Folch, 2012; Lin et al., 2012). A recent example of the use of the PUFF model for the simulation of explosive eruptions in Sakurajima volcano shows a satisfactory outcome. This model was applied to cases of explosive eruptions in 2017 and 2018 to assess its utility in forecasting real-time ash fallout. Both simulations agreed well with the measurement, which were recorded by the instruments installed at several points nearby the volcano (Tanaka and Iguchi, 2019). Here, we construct the model using many random variables $r_i(t)$, where $i = 1 \sim M$ and M is the total number of particles. $r_i(t) = (x, y, z)$ represents the position vector for the i^{th} particle at time t with its origin at the volcano vent. Using the discrete-time increment $\Delta t = 300$ s, the governing equation can be written as:

$$\begin{cases} r_i(0) = S_i, & i = 1 \sim M, \text{ for } t = 0, \\ r_i(t + \Delta t) = r_i(t) + V\Delta t + Z\Delta t + G\Delta t, & i = 1 \sim M, \text{ for } t > 0 \end{cases} \quad (1)$$

where S_i is the initial location of all the particles at the vent, $V = (u, v)$ is a vector for the wind velocity moving the particles and $Z = (c_h, c_h, c_v)$ is a vector for the diffusion velocity containing the diffusion speeds generated by Gaussian random numbers. $G = (0,0, -w_t)$ is the gravitational fallout velocity obtained by approximating the extended Stokes law for various particle sizes (Tanaka, 1994; Tanaka and Yamamoto, 2002). The movement of particles steers the diffusion Z Z-direction, and the size of the particles affects the gravitational fallout G (Searcy et al., 1998; Tanaka, 1994). The diffusion speed c (c_h or c_v) was obtained by the random walk process related to the diffusion coefficient K as $c = \sqrt{2K/\Delta t}$ (Tanaka et al., 2016; Tanaka and Iguchi, 2019). Tanaka and Yamamoto (2002) conducted several diffusion tests with various values of K, and compared the results with satellite images of actual dispersals from several volcanic eruptions in the past. Based on this research, we assigned a suitable horizontal diffusion coefficient $K_h = 150$ m^2s^{-1} and vertical diffusion coefficient $K_v = 1.5$ m^2s^{-1} as mentioned in Table 1.

Table 1. Input values for the simulations used in this study.

Eruption Source Parameters	Value
Mean Estimated Eruption Mass ($\times 10^{10}$kg)	1.1
Mass Eruption Rate, ε (kg/h)	5.8×10^{6} (Min) - 2.7×10^{10} (Max)
Horizontal Diffusion Coefficient, K_h (m/s)	150
Vertical Diffusion Coefficient, K_v (m/s)	1.5
Log-Scale Mean Grain Size (mm)	1.0

These diffusion coefficients are consistent with the in situ observations documented by Eliasson et al. (2014) and adjusted for the Sakurajima volcano. The values used in this study follow those reported by Tanaka et al. (2016, 2019) but are smaller than those reported by Fero et al. (2008, 2009) and Kratzmann et al. (2010). To further investigate the ash dispersal process to distal locations in entire Japan, we extended the simulation period of the PUFF model to 96 h after the eruption began. Following Eq. (1), by modelling the source location of the volcano vent as $S(x, y, z)$, we can adjust the number of particles released at each time step to obtain the optimal statistical information from the model. For each time step, we assigned a Gaussian random number for each particle (M_0) and scaled it according to the emission rate, making the value of the total number of particles (M) changes linearly with the emission rate (Tanaka et al., 2016). We assigned the initial number of particles to 5000 due to constraints in the available computational power. The size of volcanic ash varies from fine ash to boulders, as large particles tend to settle out quickly and then become smaller with time. Because of this process, each ash particle will have a different grain size (Bonadonna et al., 1998), and we assume that each particle has an initial grain size of a logarithmic Gaussian distribution with a standard deviation of 2.0 centred at -3.0. Thus, the average particle size was approximately 1.0 mm on a log scale, with 68% of the particles are within the range of 10 μm–10 cm, as shown in Table 1. Given the initial vertical velocity of the emission with specified damping (e-folding) time τ_0, the particles are distributed randomly in a vertical manner from the vent z_1 to the plume's peak z_2 continually. Then, using time integration for the vertical velocity in the momentum equation, we obtained the final form as $z(0) = z_1$ and $z(t) = z_2$ during the time step Δt (Tanaka et al., 2016).

3.2 Estimation on mass eruption rate based on plume heights transition

In this study, we used the estimated emission rate from the calculation done by Iguchi (2014), based on a previous study (Kobayashi, 1982). As shown in Fig. 3, we consider the maximum estimated plume height at 17,890 m around midnight on 13 January 1914 which is close to the range of plume heights in the chronicles explained in Section 2. We obtain the value of mass eruption rate (ε) and the mean eruption mass (see Table 1) with the help of temporal change in plume height. The obtained values agreed well with a recent observation (Todde et al., 2017). The pressure of the reservoir that ejects gas through a nozzle ($P_{(t)}$) at time *t* decays exponentially with time (Nishimura, 1998) following Eq. (2):

$$P_{(t)} = \Delta P_0 \left[1 + \frac{\gamma-1}{2}\left(\frac{2}{\gamma+1}\right)^{\frac{\gamma+1}{2(\gamma-1)}} v_0 \frac{A}{Vol} t\right]^{\frac{-2\gamma}{\gamma-1}} \quad (2)$$

where Vol is the volume of the reservoir, A is the cross-sectional area of the nozzle, v_0 is the initial ejection velocity, P_0 is the initial pressure, and γ is the specific heat ratio (values within the range 1.01-1.4). Because the Taisho eruption is a Plinian eruption, the plume height (H) was proportional to a quarter of the power of the heat discharge rate ($\frac{dQ}{dt}$) (Morton et al., 1956). Assuming that the volume of the reservoir is much larger than the ejected gas volume, the mass eruption rate (ε) is equivalent to the decay rate of the pressure ($\frac{dP}{dt}$), which can be estimated from the changes in plume height as follows:

$$H \propto \left(\frac{dQ}{dt}\right)^{1/4} \propto (\varepsilon)^{1/4} = k\left(\frac{dP}{dt}\right)^{1/4} \quad (3)$$

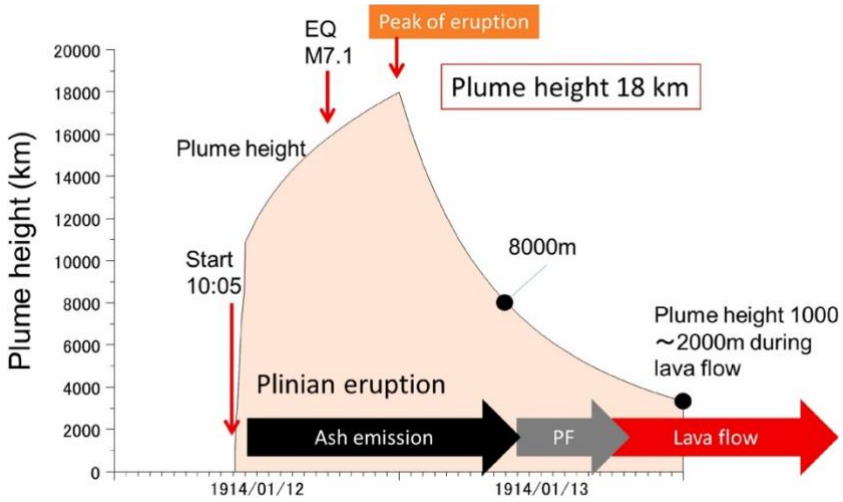

Figure 3. Plume height progression during the Taisho eruption on 12-13 January 1914 with information on both subsequent events and materials ejected (Takebayashi et al., 2021).

3.3 Long-term wind field

To conduct a long-term ash transport simulation, the long-term weather data from meteorological reanalysis values are necessary, as the wind characteristics strongly affect the sedimentary properties of the volcanic ashfall (Hattori et al., 2013, 2016; Poulidis et al., 2018). One of the available long-period historical dataset is the JRA-55 reanalysis dataset. These data contain the global meteorological reanalysis dataset from 1958 to the present, developed by the Japan Meteorological Agency (JMA) to study long-term variations in atmospheric and climate phenomena. The JRA-55 employs a reduced Gaussian horizontal grid system and applies a vertically conservative semi-Lagrangian advection scheme (Kobayashi et al., 2015). We utilised the JRA-55 data for the PUFF model, considering the horizontal wind grid to be 1.25° × 1.25°. We employed 16 vertical layers from 1000 hPa to 10 hPa atmospheric pressure, and we used this data at four different times (00, 06, 12, and 18 UTC) daily. The 3D wind field consisted of zonal wind (*U*), meridional wind (*V*), and geo-potential height (*gph*), which were interpolated to the position of each ash particle using the cubic spline method in space and time.

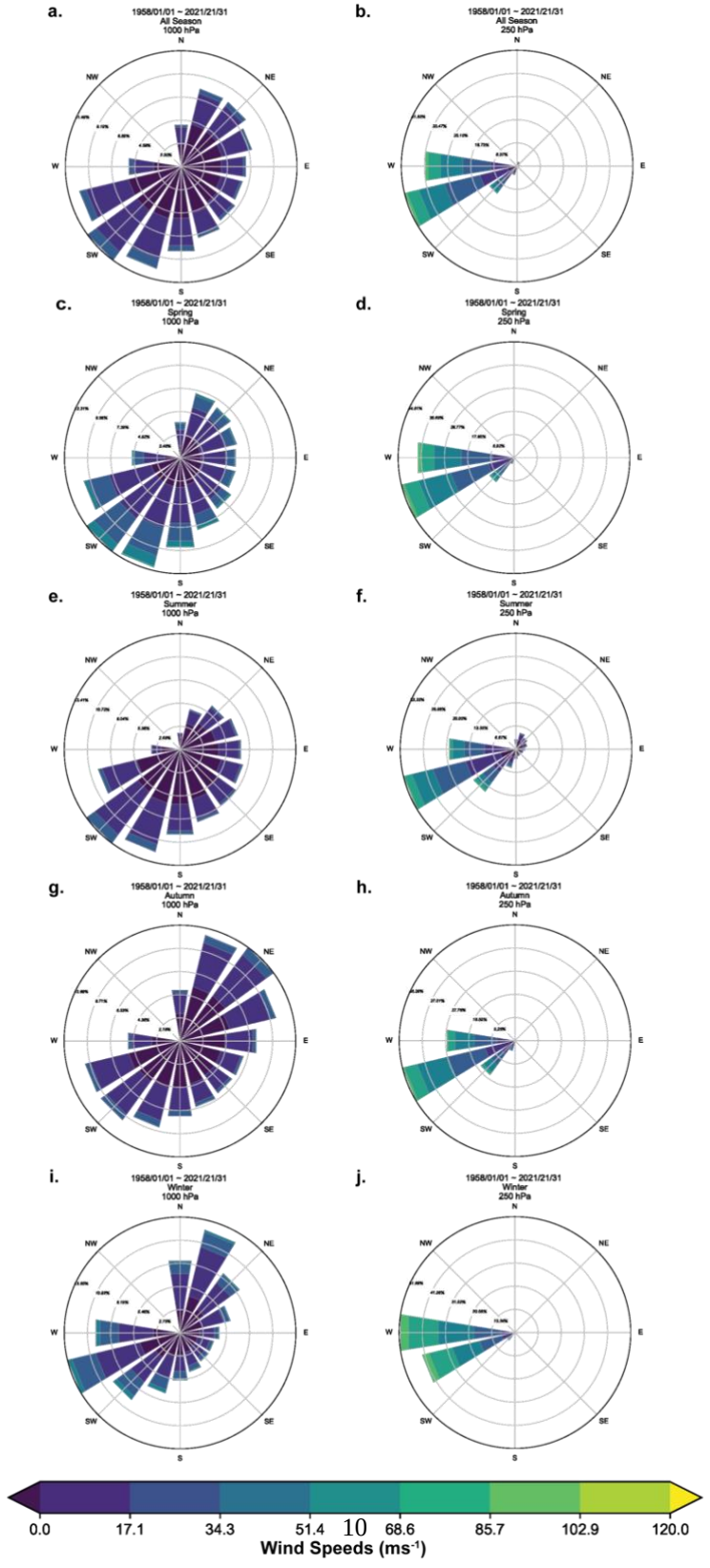
a.
1958/01/01 – 2021/21/31
All Season
1000 hPa
b.
1958/01/01 – 2021/21/31
All Season
250 hPa
c.
1958/01/01 – 2021/21/31
Spring
1000 hPa
d.
1958/01/01 – 2021/21/31
Spring
250 hPa
e.
1958/01/01 – 2021/21/31
Summer
1000 hPa
f.
1958/01/01 – 2021/21/31
Summer
250 hPa
g.
1958/01/01 – 2021/21/31
Autumn
1000 hPa
h.
1958/01/01 – 2021/21/31
Autumn
250 hPa
i.
1958/01/01 – 2021/21/31
Winter
1000 hPa
j.
1958/01/01 – 2021/21/31
Winter
250 hPa
N
NE
E
SE
S
SW
W
NW
0.0
17.1
34.3
51.4
68.6
85.7
102.9
120.0
Wind Speeds (ms-1)

Figure 4. The ten wind roses illustrate the wind conditions inferred from the JRA-55 Reanalysis dataset (Kobayashi et al., 2015) for both surface winds (first column) and upper altitude winds at approximately 10 km asl (second column). The first row ((a) and (b)) portrays all wind conditions for the entire 1958-2020, while the rest shows the influence of seasonality. (c) and (d) are the wind conditions in spring, (e) and (f) are the wind conditions in summer, (g) and (h) are the wind conditions in autumn, and (i) and (j) are the wind conditions in winter. Roses correspond to the probability of the provenance and sequential colours indicating the speed gradients.

In Fig. 4, each wind rose corresponding to the probability of the provenance identified by sectors, and sequential colours mark the speed gradients. As discussed in Sect 2, the ashfall dispersal from the Taisho eruption was controlled by both surface winds (1000 hPa) and westerlies (250 hPa). We only portrayed the wind conditions at those pressure levels, with the first column indicating the upper altitude winds and the second column indicating the latter. The second row onwards reflects seasonal variations: spring (March to May), summer (June to August), autumn (September to November), and winter (December to February), whereas the first row displaying all the dates selected for the simulation (1958-2021). As noted by previous research concerning the climatological conditions in the Sakurajima area, wind conditions change heavily depending on the season. Thus, the ash deposition process largely depends on the time of the eruption (Biass et al., 2017; Poulidis and Takemi, 2017; Poulidis et al., 2018)

3.4 Recording ashfall location and thickness

This study considers the ashfall deposits on the ground as particles with non-positive altitudes, with their location marked as a longitude-latitude pair. For each simulation, as the computation progressed, the particles with a negative value in the altitude dimension were subset to other files before being compiled when the simulation was completed. During this process, we captured the rest of the flowing particles as airborne ash concentrations, copied them to different files, and saved them using time marking every 90 minutes. We separated the measurement of the ashfall deposit and airborne ash concentrations into two different files using this mechanism. Furthermore, we measured the ashfall thickness (ashfall depth) by dividing the surface area by the ashfall density according to its particle size. First, we allocated the ashfall particles to grids according to their location. Then, we set all ashfall particles in those grids according to their average values. We considered all the adjacent grids and the pre-assigned mass values multiplied by the number of particles to obtain the total mass of the ashfall deposit. It is possible to obtain the mass of each particle based on the particle size. However, because we deliberately designate the total initial number of particles as a constant number and smaller than the actual number in the real case, the total mass of all particles is less than the actual mass, and the difference may increase as the scale of the eruption increases. Therefore, considering the particle size under the total mass conservation, the virtual mass of each particle is necessary (Shimbori et al., 2009). When the eruption reached its peak, each ash particle contained approximately 450 tons of virtual mass. This method was performed to alleviate the uncertainty that appeared when assigning a small number of particles in the simulation (see Scollo et al., 2011). After assigning the virtual mass to each particle in one grid, the thickness of the ashfall χ_{ij} at grid i, j obtained from the following equation:

$$\chi_{ij} = \sum_n \frac{\tilde{m}(D_n)}{\Delta x \Delta y} \quad (4)$$

where $\tilde{m}$ is the total virtual mass for the total n particles within the grid i, j of area $\Delta x \Delta y$ corresponding to the particle size D_n (Shimbori et al., 2009). All computations from running the simulation, processing wind fields, and computing the total ashfall accumulation on the ground were performed with a small workstation with 32GB RAM, dual 16-cores Intel Xeon E5-2620V4 2.10 GHz processors, and 4GB NVIDIA Quadro P1000 GPU.

4. Dataset overview and usage examples

4.1 Data description and availability

The dataset contains three data:

1. Ashfall deposit measurements from 128.5° E to 148.6° E, and 30.0° N to 45.9° N in 0.1°×0.1° grid (~10 km^2) for an extended period (1958-2021).
2. Ashfall deposit measurements from 129° E to 132° E, and 30.5° N to 32.5° N in 0.01°×0.01° grid (~1 km^2) for an extended period (1958-2021).
3. The time series collection of the total airborne ash concentrations in the air was recorded for every 90 minutes for an extended period (1958-2021).

To ensure maximum availability for the diverse users of the dataset, we prepared the dataset in two formats. We stored the dataset as a space-separated ASCII value table in comma-separated value (CSV) format (see Table 2) and a multi-dimensional array structure in the Network Common Data Format (NetCDF). NetCDF is useful for supporting access to diverse types of scientific data, and its files are self-describing, network-transparent, directly accessible, and extensible (Unidata, 2021). We developed the NetCDF files using the *Xarray* library in Python using the NETCDF4 package (Hoyer and Hamman, 2017). Owing to the high dimensionality of the airborne ash concentrations, we only provided these data in the NetCDF format. Meanwhile, the ashfall deposit data are available in CSV and NetCDF formats.

Table 2: The tabular view of the sample deposit data for both regions. Each column is separated by a comma, corresponding to the CSV format.

Deposit/CSV/Japan/<YYYY>/<YYYYMMDD.csv>			***Deposit/CSV/Kagoshima/<YYYY>/<YYYYMMDD.csv>***		
latitude	**longitude**	**deposit**	**latitude**	**longitude**	**deposit**
30.00	128.50	0.00	30.00	129.00	0.00
30.00	128.60	0.10	30.00	129.01	0.10
…	…	…	…	…	…
30.10	128.50	0.20	30.01	129.00	0.20
30.10	128.60	0.30	30.01	129.01	0.30
%.2f	*%.2f*	*%.2f*	*%.2f*	*%.2f*	*%.2f*

We set the name of each dataset file as the simulation date in ISO-8601 format (*YYYYMMDD*<<*.csv, .nc*>>), stored inside a directory named by year (*YYYY*) within each respective region (Japan and Kagoshima). In addition, each dataset contains an ordered set of location markings (longitude, latitude) and ashfall depth (in cm), which are stored in two decimal floating-point formats. The set of location markings is the coordinates in the NetCDF data format of the ashfall deposit data.In contrast to the deposit data, the collection of airborne ash concentrations provides the total number of particles at a specific location and time. The tracking period of the ash particles started 90 minutes after the simulation and was completed after 96 h. As the three-dimensional shape of the affected area and the total number of particles change throughout the time dimension, we assign *date_time* as the primary coordinate. The dataset directory consists of two main folders based on the data observations: *Airborne* and *Deposit*. The *Deposit* folder contains two child directories based on the data format and observation range, and then breaks down to every year starting from 1958 and ending in 2021. The *Airborne* dataset has a straightforward directory (year, *YYYY*) because it only consists of one data format, and there is no separate observational range. The detailed structure of the dataset for both the ground deposits and airborne concentrations is provided in the Appendix A.

The dataset is available at the DesignSafe-CI Data Depot (https://www.designsafe-ci.org) hosted at the Texas Advanced Computing Center (TACC). This data depot is provided by the Natural Hazards Engineering Research Infrastructure (NHERI), which provides the natural hazards engineering community and researchers with comprehensive state-of-the-art cyberinfrastructure (Rathje et al., 2017). The dataset can be accessed directly at https://www.designsafe-ci.org/data/browser/public/designsafe.storage.published/PRJ-2848v2 or through the DOI: https://www.doi.org/10.17603/ds2-vw5f-t920 (Rahadianto and Tatano, 2020). Users can access the dataset directly without any prior registration and may choose any data to be downloaded. The data can be downloaded as a single file or as a collection of multiple files. Please select the version 2 of the dataset for the latest updates.

4.2 Usage examples of the dataset

The dataset comprises ash deposits on the ground and airborne concentrations of a typical large-scale eruption at Sakurajima volcano (Sect. 2) for an extended period. Given the size of the dataset, the users can use the data to prepare a response for an ashfall disaster. Here, we demonstrate how to use these data to create conditional ashfall hazard maps. The information in such maps can serve as a reference for designing an early warning system, planning ash clean-up operations and closure management on air and land transportation, and even preparing for long-term long-distance evacuation strategies. The maps describe the probability distribution of exceeding a selected hazard threshold based on the statistical distribution of the wind profiles (Bonadonna, 2006). Several researchers used such maps to illustrate hazard assessments of a specific volcanic eruption scenario, identify the possible impacts of the assumed maximum expected events, and quantify the probability of first-order impacts on built environments (Bonadonna, 2006; Biass et al., 2014, 2016). Figure 5 reveals the conditional ashfall hazard maps accounting for the airport closure risk of all of Japan for all the wind profiles used in the simulation.

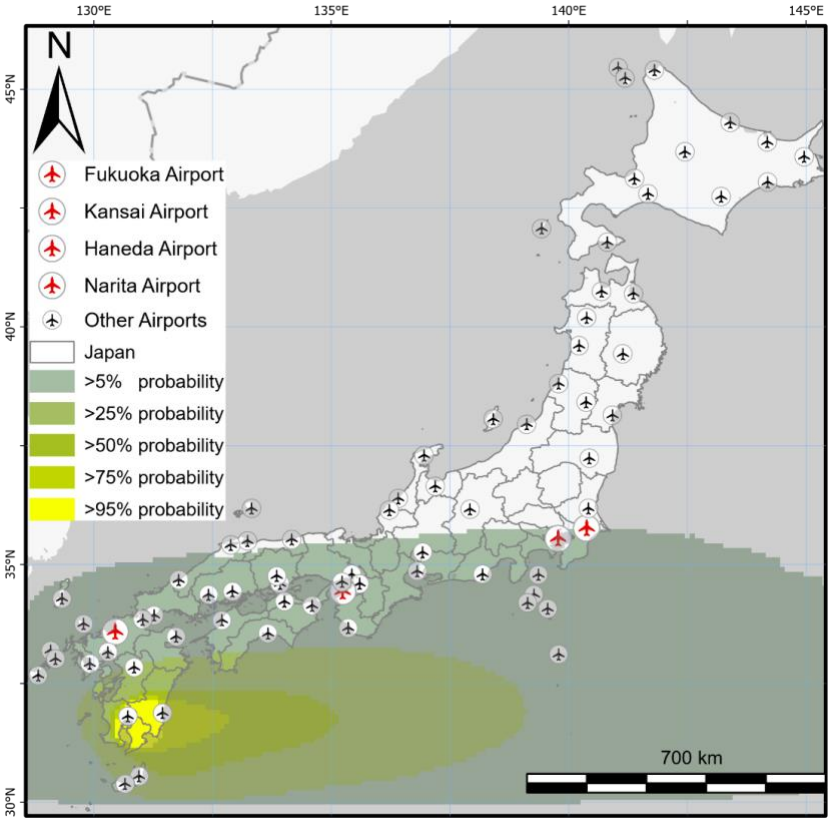

Figure 5. The probability distribution of ash dispersal with the threshold for airport closure risk (>= 0.02 cm). Airport locations are marked by black aeroplane icons on the map and the busiest airports shown larger in red icon. The colour gradient shows the difference in the probability of ash deposits exceeding the threshold. Human geography base is used as the basemap for this figure (ESRI, 2022).

We used a 0.02 cm threshold as the hazardous limit for the airport's runway that would disrupt the take-offs and landing sequence of aeroplanes, as defined by the Cabinet Office's Working Group on Wide-Area Ashfall Countermeasure at the time of Large Eruptions, Government of Japan (2018). Airport locations are marked by aeroplane icons on the map in black, and the busiest airports in Japan (Fukuoka, Kansai, Haneda, and Narita) are shown larger in red icons (Ministry of Land, Infrastructure, and Tourism, 2022). The figure illustrates how a large-scale eruption in Sakurajima volcano would affect a lot of airports from the south to the east, with the busiest airports would have more than a 5% probability of closure after an eruption, possibly displacing a numerous passengers and inflicting tremendous economic losses. The dataset can also be used to portray more prevalent information by showing the seasonal inclination on airport closure risk, as shown in Fig. 6. For example, a large eruption during summer would bring the greatest impact in terms of the number of airports, and an eruption at autumn would disrupt a high number of traffics of Japan's busiest airports. Furthermore, the airborne concentrations data can derive further extended analysis on the timing of ash arrival in some airports that would present knowledge on how to do protection or even an evacuation of aircraft if there are sufficient time windows.

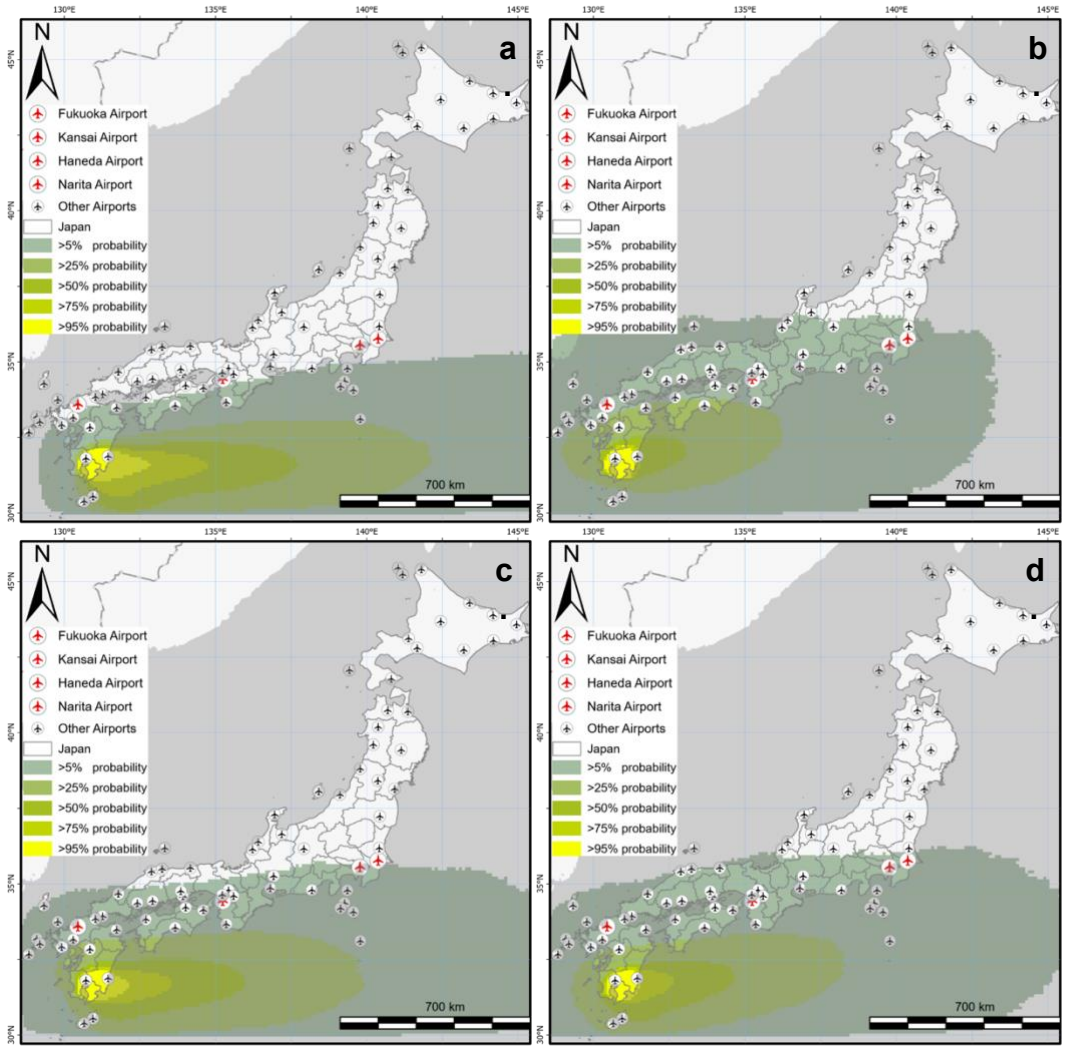

Figure 6. Seasonal probability distribution of ash dispersal with the threshold for airport closure risk (>= 0.02 cm). The panels show the probability distribution of ash dispersal during (a) winter, (b) summer, (c) spring and (d) autumn. Airports locations are marked by black aeroplane icons on the map and the busiest airports shown larger in red icon. The colour gradient shows the difference in the probability of ash deposits exceeding the threshold. Human geography base is used as the basemap for this figure (ESRI, 2022).

The variety of geographical dimensions offered by the dataset also expands the opportunity to investigate the immediate consequences of ground ashfall deposits in the proximal urban areas surrounding Sakurajima volcano. Figure 7 displays the conditional ashfall hazard maps accounting for the airport closure risk of all of Japan for all the wind profiles used in the simulation. We use a 3 cm threshold as the hazardous limit for the closures of roads and railways, as it would make them impassable by cars and trains, as defined by the Cabinet Office's Working Group on Wide-Area Ashfall Countermeasure at the time of Large Eruptions, Government of Japan (2018).

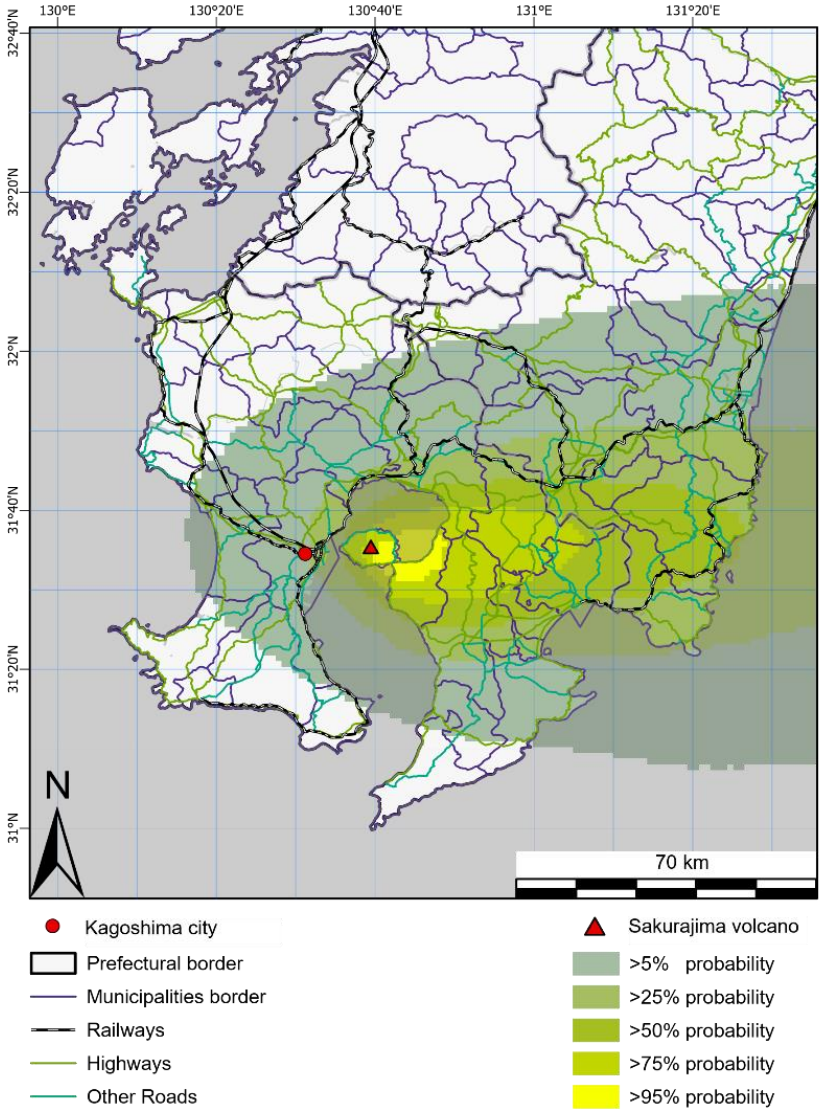

Figure 7. The probability distribution of ash dispersal with the threshold for road closure risk (>= 3 cm). Black and white stripes mark railways on the map, and highways and other roads are in coloured lines. The colour gradient shows the difference in the probability of ash deposits exceeding the threshold. Human geography base is used as the basemap for this figure (ESRI, 2022).

The figure illustrates how a large-scale eruption in Sakurajima volcano can severely affect the eastern parts of Kagoshima City, located downwind of the volcano with more than 25% probability, regardless of eruption time. The data also show how the seasonal patterns determine the extent of the ash deposits in the western parts of South Kyushu, with a summer eruption escalating the damage to almost the entire Kagoshima Prefecture, as depicted in Fig. 8. The intensity of the ashfall hazards to the transportation networks can provide ~~necessary~~ insights for preparing responses and countermeasures.

These preparations include scheduling roads and highway blockages, making evacuation strategies for safer areas, managing the ash cleaning process shortly after the eruption, and many more.

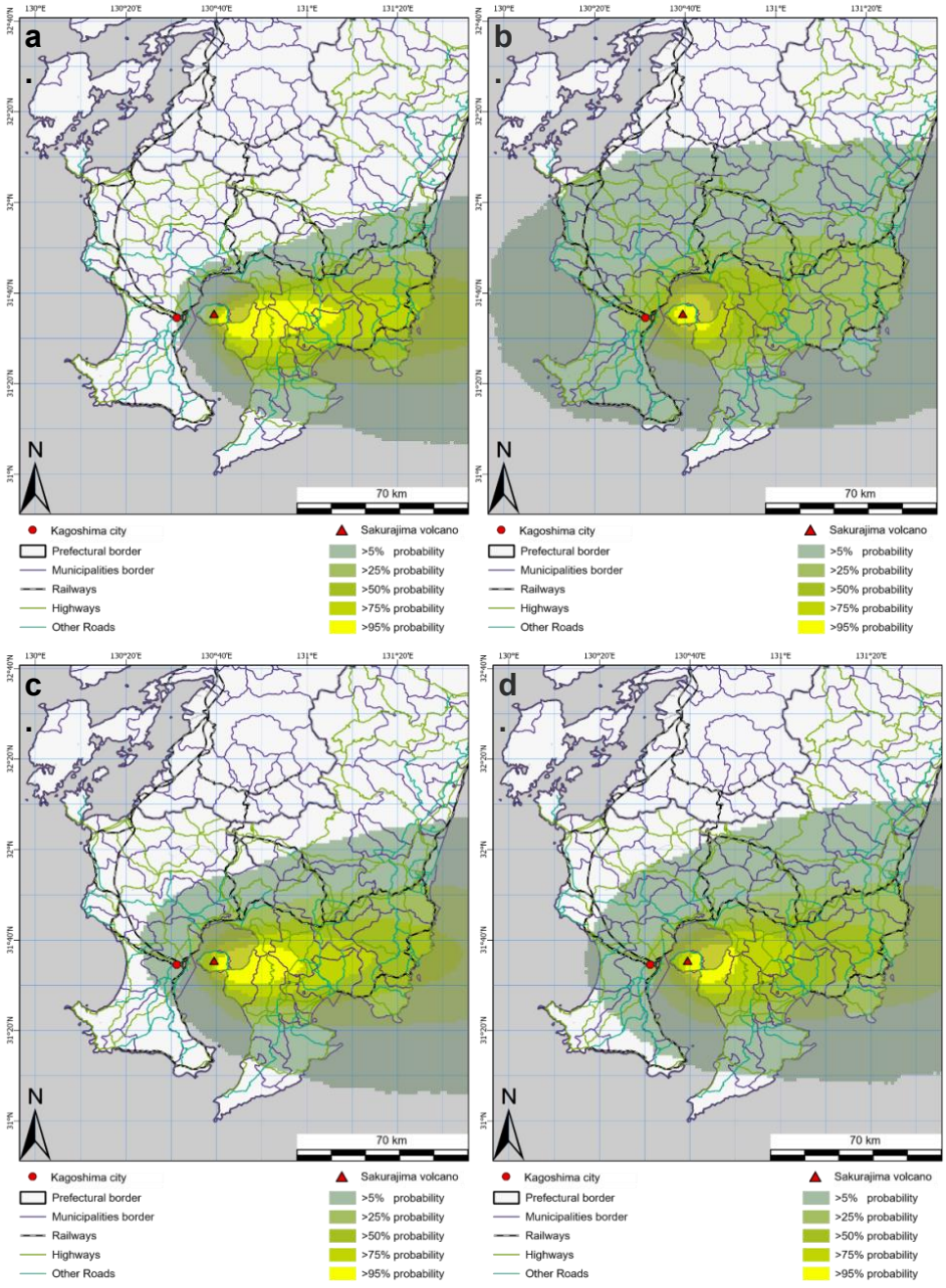

Figure 8. Seasonal probability distribution of ash dispersal with the threshold for road closure risk (>=3 cm). The panels show the probability distribution of ash dispersal during (a) winter, (b) summer, (c) spring and (d) autumn. Black and white stripes mark railways on the map, and highways and other roads are in coloured lines. The colour gradient shows the difference in the probability of ash deposits exceeding the threshold. Human geography base is used as the basemap for this figure (ESRI, 2022).

5 Validation and limitations

5.1 Validation result

Section 3.1 briefly describes the strength and the well-known performance of the PUFF model for ash dispersal simulations. Several researchers validated their simulation results through various methods, such as direct comparison to post-event reports, matching the ash clouds trajectory with satellite images, and adjusting the model's input to find the best-fit values (Fero et al., 2008, 2009; Folch, 2012; Scollo et al., 2011; Tanaka and Iguchi, 2019; Tanaka et al., 2020; Webley and Mastin, 2009). In addition, several past studies have validated ash dispersal simulations using the PUFF model for multiple eruption cases in Sakurajima volcano, albeit in smaller-scale eruptions (Tanaka and Iguchi, 2019; Tanaka et al., 2020).

For historical large-scale eruptions of Sakurajima volcano, which had larger plume height, eruption volume, and wider range of ash deposition, the validation has never been done. Ideally, if the precise wind data at the time of the selected eruption are available, we can replicate the eruption; thus, simulation results with similar wind patterns of the eruption would resemble the historical reports. The dataset presented here offered an opportunity to perform the validation of ash dispersal simulation of a large-scale eruption of Sakurajima volcano over a wide space (all of Japan). We employed the conventional method by directly comparing the selected simulation results with the available reports of the Taisho eruption. However, in this study, making a direct comparison with the ground truth was challenging owing to the following:

1. Lack of complete ground reports. Section 2 outlined the available reports gathered in cities and tobacco plantations across Japan only mentioned subjective ash deposit observations without a quantitative measurement, e.g., "frost-like ash", "house roof become white", and "slight deposit".
2. Complete wind data at the time of eruption were absent. Only surface observation are available at limited observation points, and it is not possible to completely replicate the ash transport process.

Despite these limitations, we attempted to utilise an innovative approach to present a validation result using the dataset presented here with all available information. The ash dispersal map presented in Fig. 2 provided the locations of the ash deposition to all of Japan is the. Moreover, the detailed weather conditions that asserts control over the ash dispersal process are available as well. Therefore, we utilised ~~to~~ these information to proceed with the validation process, as follows:

1. Manifesting the ground data in the same dimension as the simulation output by digitally redrawing the ash distribution map for all of Japan, provided by Omori (1914), using available geographic information software (GIS). This procedure produced a new ground observation data that resembled the original ash distribution of the Taisho eruption.
2. The equivalent wind pattern on the day of the eruption was found for similar weather on the wind data we used in this study, JRA-55 Reanalysis. We expected that the similarity in weather features would also bear a similarity in the wind profile across multiple atmospheric levels. This process subsets the number of simulation results for validation checking with the data produced in the previous step.

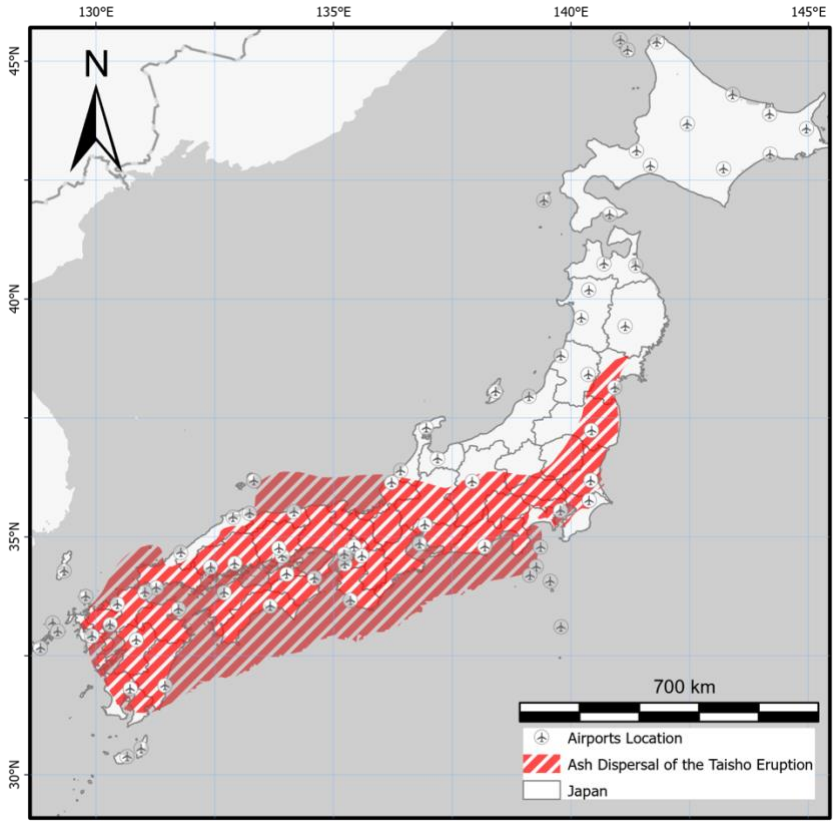

Figure 9. Transformed ash dispersal map using ArcGIS software with airport icon as impacts reference. Human geography base is used as the basemap for this figure (ESRI, 2022).

The detailed explanation of each step is presented in Appendix B. Figure 9 portrays the transformed ash distribution map that has same dimension with simulation results, and Table B3 display the top 10 dates which are considered to have similar weather conditions with the weather during the eruption. Once we determined all the required components, we performed the matching mechanism between the simulation result of the chosen date(s) and the new ground data. The matching is performed through a binary contingency matrix.

Table 3. The binary contingency table for the validation process.

Actual Ash Precipitation of the *Taisho* Eruption	**Selected Simulation Results**	
	Affected	*Unaffected*
Affected	**TP**	**FN**
Unaffected	**FP**	**TN**

Table 3 briefly explains the contingency table used to evaluate the simulation results. The evaluation focused on measuring how the ash dispersal map produced from the simulation on selected dates would equally cover an equivalent region of interest to the ground data.

We limited the evaluation for all ash deposits on the land, and omitting all ash deposit on the sea. Then, by matching the binary contingency table, we quantified the hit rate score Hit of the simulation result as follows:

$$Hit = \frac{TP+TN}{TP+TN+FP+FN} \quad (4)$$

TP denotes the true positive, which means that both the ground data and the simulation results have an ash deposit on the same grid points (affected). *TN* denotes the true negative, in which the ground data and the simulation results don't have an ash deposit on the same grid points (unaffected). Meanwhile, *FN* denotes the false negative, in which particular grid points are marked as unaffected in the simulation results but appear to be affected in the ground data. In reverse, *FP* denotes the false positive, in which particular grid points are marked as affected in the simulation results but appear to be unaffected in the ground data. Therefore, the hit rate score *Hit* is the simulation result correctly dispersed ashes to the same grid points as the ground data, divided by all defined grid points from the original ash dispersal map. To make it brief, we chose only the top date of the STS scores list in Table B2 (5 March 1997) in the matching process. The simulation results of the chosen date reached satisfactory performance with a high *Hit* score (0.832). This result means that the selected date with weather conditions similar to those of the Taisho eruption have a considerable identical ash dispersal pattern.

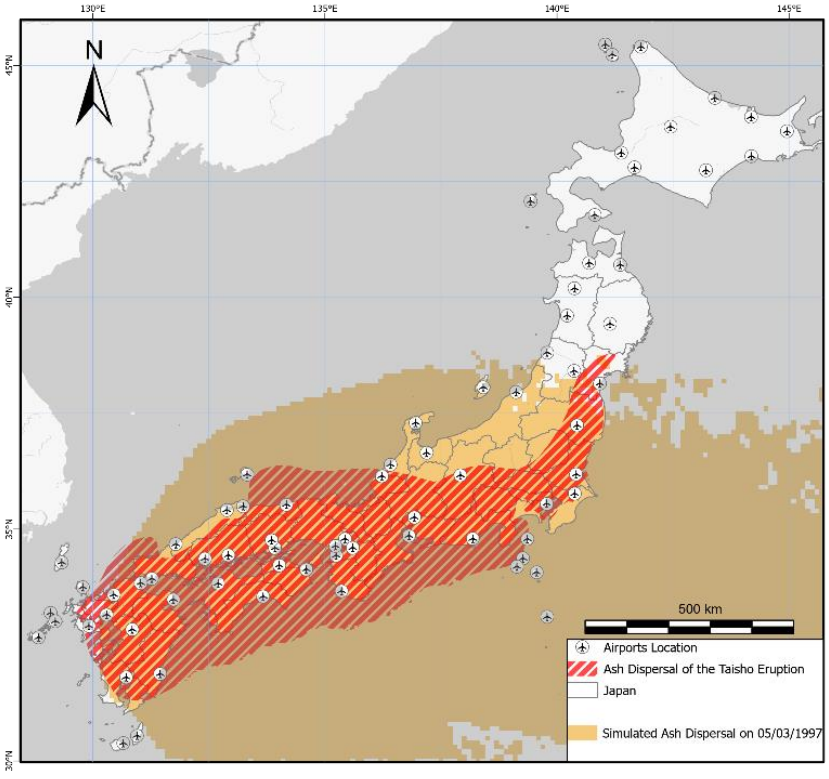

Figure 10. The comparison of the ash distribution coverage between the original ash dispersal map and the simulation results on the selected date (5 March 1997). The red-stripped area indicates the original areas affected by the Taisho eruption, and the light orange colour represents the ash dispersal from the simulation. Human geography base is used as the basemap for this figure (ESRI, 2022).

Figure 10 further exhibit the evidence of the similarities in the ash dispersal map for the selected simulation results. The process to produce such a result involve a complex procedure (detailed in Appendix B) because of the limited availability of the necessary components for the direct comparison. Because of this complication, such a process may not yield perfect results, both for the checking components (new ground data and selected wind patterns due to similar weather conditions) and the matching ash distribution of the simulation.

5.2 Dataset limitations

Generally, the ash deposition results from the simulation of volcanic ash dispersal and transport models rely on how the parameters values of both eruption source parameters and the wind conditions during the eruption are set. These parameters are critical in determining the impacts of ashfall on proximal and distal locations (Bonadonna et al., 2012; Folch, 2012; Macedonio et al., 2016; Mastin et al., 2009; Webley and Mastin, 2009). This study used the deterministic value of plume height, erupted mass, and mass eruption rate as the eruption source parameters. We utilised the calculation by Iguchi (2014), incorporating the study by Morton et al. (1956) for the relationship between the observed plume height in the historical reports and studies (Kobayashi, 1982; Koto, 1916; Omori, 1914; Todde et al., 2017) to produce the mass eruption rate. There was a positive correlation between the change in plume height over time and both the total eruption mass and mass eruption rate. However, we advise caution when using this method, as it introduces a significant bias in the mean height value. The eruption rate is roughly proportional to the fourth power of height. Therefore, error in assigning the precise height will significantly affect its conversion to the eruption rate (Folch et al., 2012; Mastin et al., 2009). We assign the parameters of the last eruption as a baseline of the largest eruption size or plume height as a conservative safety factor, although we recognise wide variability that could change the significance of the implied hazard. The values used in this study agreed well with the past observations, and the bias presented in the eruption source parameter should be small and would not significantly affect the ash dispersal mechanism. However, variations in these parameters can result in different eruption rates and total mass, resulting in different ashfall footprints. In addition, future vent location, eruption style and size, and eruption duration significantly affect the impacts of the ashfall in both proximal and distal areas (Bonadonna et al., 2012; Mastin et al., 2009; Selva et al., 2018). Furthermore, depending on the model, the parameters which need to be set arbitrarily, such as the diffusion coefficient, settling particle velocity law (see Table 1), orographic effects, and the lack of topographical data, could cause discrepancies if different variations were used (Macedonio et al., 2016; Poulidis et al., 2017, 2018; Scollo et al., 2011). Finally, the distribution of the total grain size, the particle density and shape, and the chosen aggregation method also affect the accuracy of the model outputs (Bonadonna et al., 2012; Folch et al., 2010, 2012; Mastin et al., 2009; Selva et al., 2018). Here, we approach the simulation with the main purpose of characterising the Taisho eruption, which eliminates the variations in those variables because we used a fixed scenario as the worst case.

We acknowledged the limitations of this study, which used the fixed values for the eruption source parameters to precisely replicate the transition in the Taisho eruption, which strongly restricts the various possibilities of future events. Following the result mentioned earlier by Hickey et al. (2016), which illustrates how the current uplift situation is similar to that of the preceding eruption event, our results could provide valuable input to both authorities and stakeholders. The dataset presented here will provide a guideline for an insightful understanding of how such a large explosive eruption would affect contemporary Japan. Moreover, inaccuracies can occur due to the effects of the winds and atmospheric humidity, among other factors (Folch et al., 2012; Mastin et al., 2009). Meteorological conditions determine the ashfall dispersion trajectory and ashfall deposit location (Macedonio et al., 2016). Therefore, reanalysis datasets are favourable for use because they have better accuracy than the forecast ones (Folch et al., 2012). It should be noted that the variability in the different meteorological databases (e.g., ERA-Interim, JRA-55, NARR, etc.) is relatively insignificant (Selva et al., 2018). As intended to provide guidance for a worst case scenario, the dataset provided can remain helpful in extending the present study toward the ashfall risk analysis and its decision-making process. We argue that the dataset here is vital to support future researchers and emergency managers in analysing and planning crisis responses under different conditions. It is important to note that these assignments are rough estimates of one of the possibilities for the most likely future eruption size and type at Sakurajima volcano. We understand that there might be inconsistencies in the dataset that likely introduces a bias in the ashfall hazard and risk analyses. Future users should consider all these sources of uncertainty.

6 Conclusion

Ash dispersal products from large eruptions have devastating impacts on various sectors, both in areas near the volcano and in distal locations. Emergency managers and crisis response planners need to acknowledge the compounded effect of ashfall deposits on the infrastructures to manage losses appropriately. This study presents a dataset that is useful for more extensive research and planning, focusing on the context of the entire country. This paper describes the complete generation process of a dataset based on the recent large eruption of Sakurajima volcano (the Taisho eruption) by replicating the eruption process over an extended period from 1958 to 2021. Furthermore, we added a validation result of ash dispersal simulation of a large-scale eruption of Sakurajima volcano over a wide space (all of Japan) using the selected simulation results from the dataset. The complications and constraints of the validation procedure have been acknowledged. Finally, we acknowledge the limitations and uncertainties of the dataset. Although it contains some degree of inaccuracies, the dataset can still encourage further studies in the ashfall risk analysis and decision-making process as limited as possible. Such advancements will be crucial to support future researchers and emergency managers in devising disaster responses under different conditions.

Appendix A

The structure of the dataset in the NetCDF format are shown in Fig. A1 for ground deposits data and Fig. A2 for airborne concentrations data.

Deposit/NetCDF/Japan/<YYYY>/<YYYYMMDD.nc>

▾ Coordinates:

latitude	(latitude)	float32	30.0 30.1 30.2 ... 45.7 45.8 45.9
longitude	(longitude)	float32	128.5 128.6 128.7 ... 148.5 148.6
eruption_date	()	datetime64[ns]	...

▾ Data variables:

deposit	(latitude, longitude)	float32	...

▾ Attributes:

Name :	Long-period Ashfall Deposition Dataset (1958-2021) from the Sakurajima Taisho Eruption.
Type :	Daily Ashfall Deposit for Japan region from simulation on 1958/01/01 10:00 JST (01UTC).
Description :	This dataset presents the ashfall deposit thickness in cm for Japan. The dataset generated from a numerical simulation of the 1914 Taisho eruption in Sakurajima using PUFF model and JRA-55 Reanalysis data.
Edition :	1
Authors :	Haris Rahadianto
Publisher :	Disaster Prevention Research Institue (DPRI), Kyoto University, Japan
License :	Open Data Commons Attribution License (ODC-By)

Deposit/NetCDF/Kagoshima/<YYYY>/<YYYYMMDD.nc>

▾ Coordinates:

latitude	(latitude)	float32	30.0 30.01 30.02 ... 32.99 33.0
longitude	(longitude)	float32	129.0 129.01 ... 131.99 132.0
eruption_date	()	datetime64[ns]	...

▾ Data variables:

deposit	(latitude, longitude)	float32	...

▾ Attributes:

Name :	Long-period Ashfall Deposition Dataset (1958-2021) from the Sakurajima Taisho Eruption.
Type :	Daily Ashfall Deposit for Kagoshima region from simulation on 1958/01/01 10:00 JST (01UTC).
Description :	This dataset presents the ashfall deposit thickness in cm for Japan. The dataset generated from a numerical simulation of the 1914 Taisho eruption in Sakurajima using PUFF model and JRA-55 Reanalysis data.
Edition :	1
Authors :	Haris Rahadianto
Publisher :	Disaster Prevention Research Institue (DPRI), Kyoto University, Japan
License :	Open Data Commons Attribution License (ODC-By)

Figure A1. The structures of the sample deposit data for both regions in the NetCDF format.

Airborne/<YYYY>/<YYYYMMDD.nc>

▾ Coordinates:

date_time	(date_time)	datetime64[ns]	1958-01-01T11:30:00 ... 1958-01-...
eruption_date	()	datetime64[ns]	...

▾ Data variables:

longitude	(date_time)	float32	...
latitude	(date_time)	float32	...
altitude	(date_time)	float32	...
ash_particles	(date_time)	float32	...

▾ Attributes:

Name :	Long-period Ashfall Deposition Dataset (1958-2021) from the Sakurajima Taisho Eruption.
Type :	Airborne Ashes for 96 hours from 1958/01/01 10:00 JST (01UTC), recorded at every 90 minutes.
Description :	This dataset presents the total number of airborne ash particles from the starting simulation date. The dataset generated from a numerical simulation of the 1914 Taisho eruption in Sakurajima using PUFF model and JRA-55 Reanalysis data.
Edition :	1
Authors :	Haris Rahadianto
Publisher :	Disaster Prevention Research Institue (DPRI), Kyoto University, Japan
License :	Open Data Commons Attribution License (ODC-By)

Figure A2. The structures of the sample airborne data in the NetCDF format.

Appendix B

The diagram explaining the flow of the validation procedure for this study is portrayed in Fig. B1

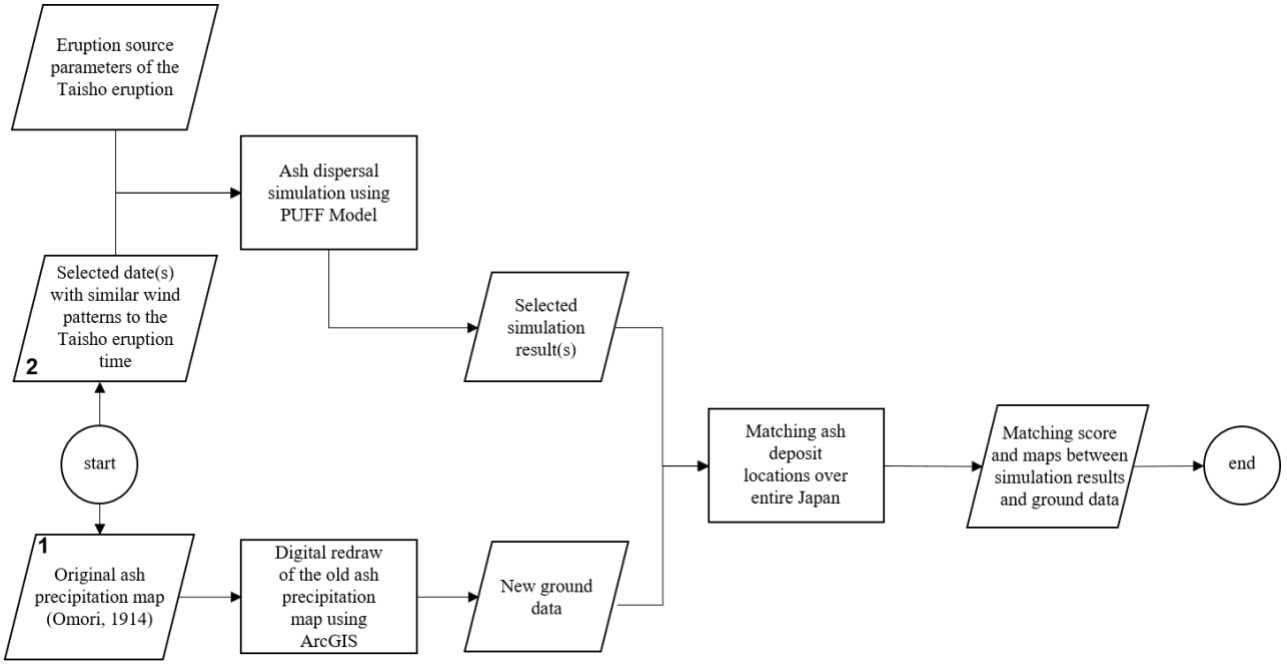

Figure B1. The flowchart of the validation procedure using the dataset produced in this paper. (1) the process of digitising the original ash precipitation map to become new ground data, and (2) the process of selecting a simulation result for matching with the ground observation data.

B.1 Transforming the original ash precipitation map

In the first step, as shown in Fig. B1, we transformed the ash dispersal map in Fig. 2 using ArcGIS software with a WGS 84 projection (ESRI, 2017). In addition, we added the current airport locations to signify the impacts of the very fine ashfall on entire Japan. We conducted the map transformation by placing binary markings to indicate the affected regions, i.e., 1 for red-stripped grids and 0 for the rest. All the binary values have a pair of longitude-latitude values to represent their positions on the map. This procedure is necessary, as we finally have a ground data in the same area dimension as the model output to directly compare it with the selected simulation result.

B.2 Finding the identical weather characteristics

After we obtained the new ground data, the next steps matching a simulation result with it. However, we cannot simply check the data with any results from the simulation because of the unusual weather at the time of the eruption. Due to the absence of a complete wind profile at the time of the eruption, we investigated the weather conditions on that day. Understanding the weather components at the time of eruption is crucial for determining the behaviour of the ash fallout trajectory. This feature of the Taisho eruption is often omitted, although it explains why the ashfall from the eruption moves erratically to distal locations. Several prior researchers did not proceed with their analysis of this anomaly, which has proven to be influential concerning the impacts in distal municipalities (e.g., Biass et al., (2017), among many others).

The Taisho eruption occurred in winter when mid-latitude cyclones were active. With the stationary planetary waves generated by the land-sea contrasts and the flow over the Himalayas, these phenomena reinforce the tropospheric jet stream and the baroclinic wave to be the strongest. In Japan, the reinforced jet streams cause the westerlies at 250 hPa pressure to exceed 70 ms^{-1}. The winds in the tropospheric jet stream blow from the west throughout the year; they are strongest in winter and weakest in summer (Wallace and Hobbs, 2006). The Meteorological Research Institute of the JMA (JMA-MRI) further clarifies how the westerly wind traverses above the Sakurajima volcano all year long from west to east. The westerlies reach their peak velocity in January and then continue to weaken until their lowest speed in summer, before rising again (Maeda et al., 2012). This cycle runs for the entire year and is one of the deciding factors for the ash dispersal pattern.

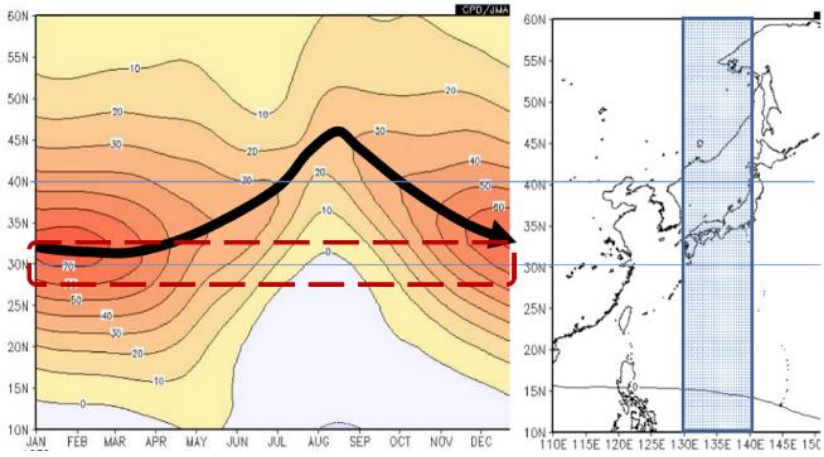

Figure B2. Seasonal progression of the westerlies over Japan at 12 km from the surface (Maeda et al., 2012). The red dashed square indicates the region covering Sakurajima volcano and Kagoshima city. The vertical axis shows the latitude degree of the wind position. The horizontal axis shows monthly changes of the westerlies velocity for the left image and the longitude of the winds on the right image. The thick black arrow from left to right indicating the location of maximum velocity of westerlies based on seasonal progression. The straight blue lines indicate all regions in Japan affected by the westerlies. The small number inside the left image is the wind contour.

Figure B2 shows a time-latitude cross-section of the east-west wind at the 250 hPa (approximately 12 km from the surface), averaged at 130°E to 140°E based on the 30-year survey (Maeda et al., 2012; Mita et al., 2018). The Sakurajima volcano and its vicinity are situated around 31° N (red dashed square), including Kagoshima City. Therefore, the westerlies would bring most of the ashfall from the eruption to the east. Instead, chronicles reported that ashes traversed to the north, west, and southwest (Omori, 1914; Todde et al., 2017). This pattern contrasted with the preceding eruption (An'ei eruption – November 1779) that followed the pattern of the westerlies (Tsukui, 2011). Research investigating the past ash dispersal patterns from Sakurajima volcano also reaffirms the differences due to seasonal features, agreeing that during winter, tephra should mostly go eastward, with most of it falling in the Pacific (Biass et al., 2017; Poulidis et al., 2018; Mita et al., 2018). When the eruption occurred, the vicinity of Kagoshima City and Sakurajima volcano experienced a maximum atmospheric pressure the first four days, providing a unique characteristic of the Taisho eruption.

From 9 January 1914 to the morning of 13 January 1914 atmospheric pressure in Japan consistently recorded an unusually high, resulting in stable sea waves and low-velocity winds, indicating calm and clear weather in most places (Omori, 1914). Unexpectedly, the weak winds helped many people living near the volcano, evacuated by boat (Kitagawa, 2015). The eruption seemed to play a significant role in increasing the temperature in Kagoshima, but apparently, it turned out to be the opposite (Omori, 1914). The leading cause of the high temperature at the time of eruption time was a sudden increase in southerly winds, as observed in Okinawa, 373 km from the vent (Omori, 1914). Furthermore, the chronicles explained the tri-daily general weather conditions during the eruption and found that similar weather phenomena also occurred on 17 January 1914 (Omori, 1914). This vital information helped us derive a method for validating our simulation results. Following such reports, we concluded that clear, sunny weather with weak winds played a major role in transporting ashfall to entire Japan, and such conditions, although rare, can be repeated. From this observation, we assume that the wind pattern will also be similar on days with identical weather characteristics as irregular as the day of the Taisho eruption. Using this assumption, we further obtained wind data at various atmospheric pressure heights matching the wind data during the eruption. Thus, the simulation on the dates with similar weather is expected to produce a similar ash distribution to all of Japan, comparable with the transformed ash dispersal map in Fig. 9.

Owing to seasonal differences, finding dates with similar weather only uses winter dates, because the Taisho eruption occurred in winter as well. In detail, we searched and found the day(s) with weather conditions like the eruption day (12 January 1914). The search process only focused on winter days (December, January, February, and March) from 1 January 1958 to 31 December 2021. The important main features to query are clear sunny days, weak winds with high atmospheric pressure (anti-cyclonic), and higher temperatures, which are quite distinct and rarely occur in Japanese winter. These features reiterate the peculiarity of the Taisho eruption and its diverging ash distribution. Weather comparisons were conducted using available weather information from the chronicles and historical weather information provided by the JMA on their website. However, the past meteorological data are limited because the Japanese authority only maintained surface weather condition (temperature, pressure, humidity, precipitation, and wind speed) in a major meteorological observatory located in the capital of selected prefectures. These past data consist of daily and hourly observations. Apart from surface observations, there are no other available measurement recorded at different atmospheric pressure levels. Other available information is the surface weather chart on the day of the eruption (12 January 1914) and all simulation dates. Therefore, we decided to utilise a surface weather chart instead of surface observations, as it provides a clearer description of a weather phenomenon on a particular day. A weather chart, also known as a weather map, usually consists of symbols and features that describe a particular meteorological pattern in a specific space-time dimension. Weather charts were created by plotting the relevant measurements such as mean sea-level pressure, wind barbs, and cloud cover. This plotting can help find synoptic-scale features, such as weather fronts. A meteorologist usually performs an isobaric analysis of these maps, which involves the construction of lines of equal mean sea level pressure (Wallace and Hobbs, 2006).

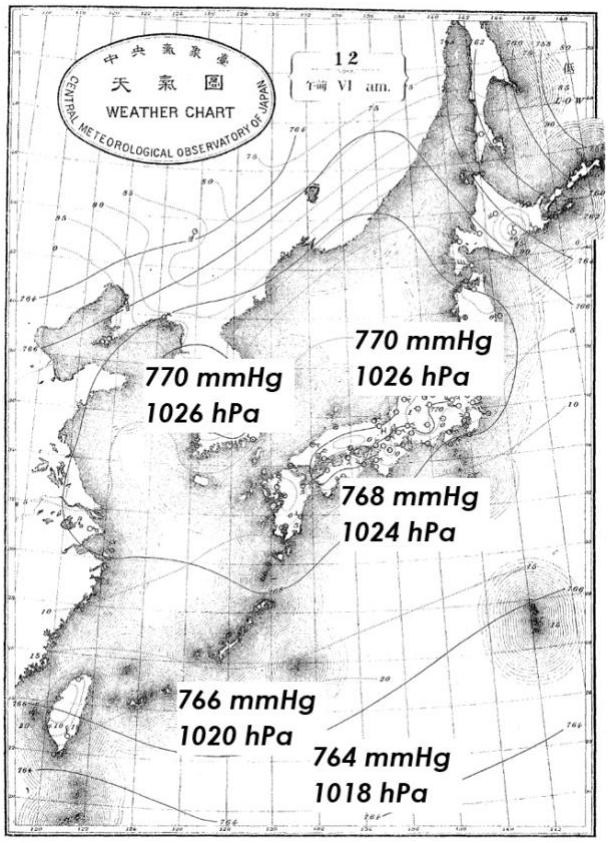

Figure B3. The weather chart on the Taisho eruption with additional markings of pressure measurement converted to the latest convention (mmHg → hPa). Modified from Omori (1914).

Figure B3 shows the weather chart at 06:00:00 on 12 January 1914, with the modern convention of pressure measurements. This weather chart displays how the high-pressure condition covers almost the entire Japan centring the central Honshu. These local maxima in the pressure field, denoted by a big "**H**" letter, can simply explain the common weather characteristics in that specific region. The wind becomes stronger when the pressure gradient between the high- and low-pressure systems increases. Land friction weakens the wind coming out from high-pressure systems. Hence, high-pressure systems typically result in weaker winds with clear skies and relatively warm weather (Wallace and Hobbs, 2006). These implications corroborate the weather reports during the eruption day. Accordingly, using the similarity on the surface weather chart is appropriate for identifying identical weather conditions.

B.2.1 Weather report commentary on the surface weather charts

Our initial attempt to search for identical weather by using weather chart similarity is by employed an image similarity method to compare features drawn in a pair of weather charts. However, this attempt turned out to be very difficult, as the weather chart on the eruption day was much different from the modern weather chart currently used in Japan.

The measurement time and scale of barometric pressure, the dimension and projection of the map, and the area included in the map were all different between the current daily weather chart and the weather chart on 12 January 1914. The format of the daily weather charts in Japan has changed several times after World War II. Starting in 1883, the JMA produced daily surface weather charts for the Asia-Pacific region, consisting of Japan and Japanese-occupied areas pre-World War II. Since August 1958, the JMA has provided daily weather charts at various upper levels (500 hPa, 700 hPa, and 850 hPa) for the Asia-Pacific and 500 hPa for the Northern Hemisphere region. Then, starting in March 1996, the JMA added a daily surface weather chart for the Northern Hemisphere and a 300 hPa level for the Asia-Pacific region. Finally, in February 1999, the JMA updated all the weather charts and added a specific surface weather chart for the regions of Japan. These changes were also accompanied by changes in the weather chart format, and the current daily weather charts follows the 1999 format. Thus, owing to the ever-changing formats of past weather charts and the modern ones, performing image similarity is not feasible and is a time-consuming task because we need to have multiple training data for every format to decide whether the two images are similar. We moved to another option which includes employing other information available in the daily weather chart. Another piece of information available inside the weather chart is the general weather report commentary (*天気概況*). Experts in meteorology developed this commentary as a guide to weather conditions during a particular day. Figure B4a portrays the weather report commentary on 12 January 1914 located at the bottom left of the second page.

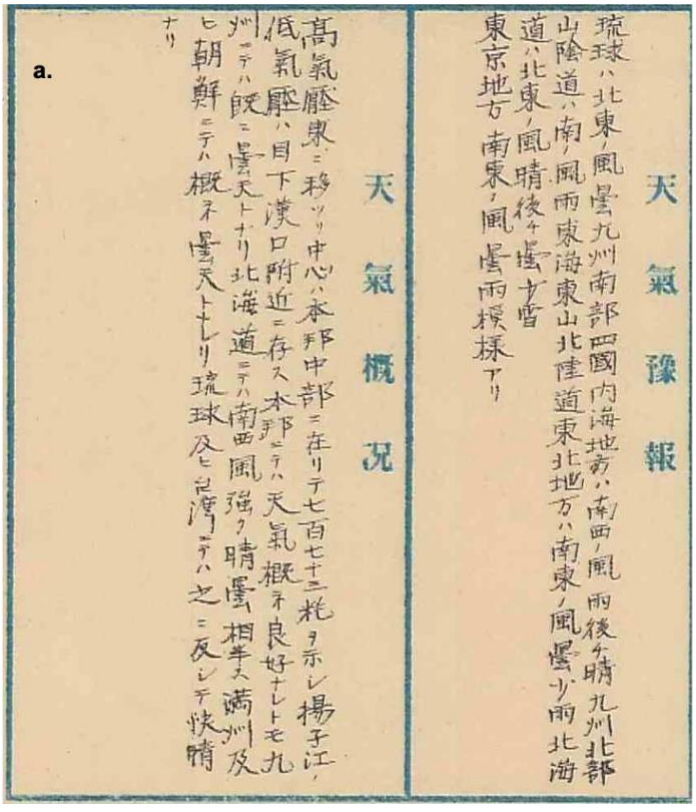

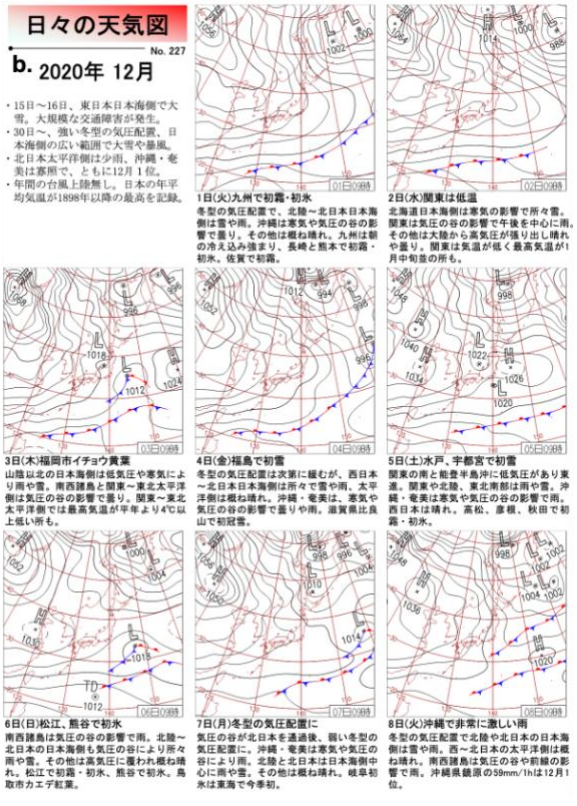

Figure B4. The general weather report commentary on the weather condition inside the weather chart. (a) The old weather chart put the commentary on the bottom of the second page on the day of the Taisho eruption (Database of Weather Charts for Hundred Years, 2022). (b) The modern weather chart mentions the commentary on the bottom of the monthly compilation of daily weather charts (Japan Meteorological Agency, 2022).

All historical daily weather charts, from 1883 up to March 1938, have a commentary written on a weather chart explaining the weather conditions. However, this feature was omitted from April 1938 until December 1995. The JMA resumed adding a general weather report commentary feature to the daily weather chart from January 1996 to date, under the weather chart images in the monthly compilation of historical daily weather charts (Database of Weather Charts for Hundred Years, 2022). Figure B4b shows the first page of the daily weather charts compilation for December 2020 from the JMA as a reference (Daily Weather Chart, 2022). The commentary usually includes the important weather characteristics on that day, such as the existence of high- or low-pressure centres or fronts, the description of extreme weather phenomena such as typhoons, heavy rains, or heavy snow, and other special events on the day, such as disasters. This description allows us to find similar weather between the dates used in the simulation and the day of the eruption, even though we further decreased the number of dates used in the searching process (1996-2021, 3120 days). However, before proceeding with the searching process, we need to perform several conversions because there is a minor distinction between the old commentary and the modern ones, which are:

1. The old commentary on the weather chart on the day of the eruption was based on old Japanese syntax.
2. The old commentary addressed both the weather in Japan and the weather in a Japanese-occupied areas.

We solve these slight differences by simply converting the old commentary to contemporary Japanese syntax and removing all observation areas outside the modern Japan region. The first column in Table B1 denotes the original form written in the Old Japanese syntax. The second column shows the transformation from the Old to the contemporary Japanese. The old commentary consists of three parts: explaining the location of high- or low-pressure centres, the weather on the main islands of Japan (Honshu, Kyushu, and Hokkaido), and lastly on other parts of the Asia-Pacific, coincidentally, at that time all regions mentioned are under Japanese occupation. This commentary agrees with the meteorological report provided in the chronicles (Omori, 1914). Therefore, we omitted the last phrases and focused only on the weather on the main islands of Japan. Then, further converted it to a form similar to the commentary in the current daily weather charts. The new phrases in the last column give more brief comments that match with the contemporary style in the modern weather charts while still maintaining the important features (high-pressure all over Japan, clear/sunny weather in main islands, Kyushu is cloudy, and Hokkaido is either clear or cloudy with strong south-westerly winds). Then, we compared these phrases in contemporary Japanese with all the commentaries found in the modern weather chart (from 1 January 1996 to 31 March 2021) provided by the JMA in winter (from January 1996 to March 2021), from the historical archive collected by the National Institute of Informatics (Database of Weather Charts for Hundred Years, 2022). These commentaries explain the weather conditions on a particular day in a random sequence, that is, not in a similar order to the processed commentary phrases (from 12 January 1914). Finally, we utilised the natural language processing (NLP) method to find semantic textual similarity between all commentaries with sentence embedding using SentenceBERT (Reimers and Gurevych, 2019).

Table B1: The conversion of the general weather commentary in the weather chart on 12 January 1914.

Original Form	Contemporary Form	Final Form
高気圧東に移り、中心本邦中部に在りて、773mm を示し。揚子江低気圧は目下漢口付近に存す。本邦にては、天気おおむね良好なれとも、九州にてはすでに曇天となり、北海道にては南西風強く晴曇相半す。満州および朝鮮にてはおおむね曇天となれり、琉球および台湾にてはこれ反して快晴なり。	*高気圧は東に移動し、日本の中心にあり、気圧計の値は 773mm を示すしている。長江にある低気圧は、ちょうど武漢付近に存在する。日本では、天気は晴れているが、九州地方では既に曇りとなっており、北海道では南西の風が強く晴れたり曇ったりしている。満州と朝鮮はおおむね曇り、琉球(沖縄)と台湾では、反して快晴。。*	*日本付近は移動性高気圧に覆われている。日本列島わ晴れ。一方、九州は曇り。北海道は南西風が吹き、晴れや、曇り。*

B.2.2 Semantic textual similarity on weather report commentary using SentenceBERT (SBERT)

To find similar weather, both commentaries should have an equivalent meaning that is semantically similar, regardless of the sentence structures and words used to form the sentence. The vast improvements in machine learning (ML) and artificial intelligence (AI), especially in NLP tasks, allow us to find the similarity between two sentences using semantic textual similarity (STS) by embedding all sentences first. Word embedding represents words in the form of a real-valued vectors. This process encodes the meaning of a word such that the words that are closer in the vector space will be similar in meaning (Jurafsky and James, 2000). Sentence embedding is simply the sum of the individual word embedding (Cer et al., 2017). STS scores semantic similarity in varying degrees (e.g., a vehicle and a car are more similar than a wave and a car) instead of binary (e.g., a vehicle and a car are the same, and a wave and a car are not the same). STS provides a unified framework that allows for the extrinsic evaluation of multiple semantic components. This framework includes word sense disambiguation and induction, lexical substitution, semantic role labelling, multi-word expression detection and handling, anaphora and co-reference resolution, time and date resolution, named-entity handling, under-specification, hedging, semantic scoping and discourse analysis (Agirre et al., 2012).

Here, we can consider a pair of sentences to be similar (in this case, the weather condition) if they are located close to each other, as both sentences are mapped to a dense vector space (Reimers and Gurevych, 2019, 2020). Google has led the current state-of-the-art NLP development with its technology, Bidirectional Encoder Representations from Transformers (BERT), which can handle various NLP tasks accurately, including question answering, sentence classification, and sentence-pair regression (Devlin et al., 2019). However, BERT is not optimal for handling several tasks, such as large-scale semantic similarity comparison, clustering, and information retrieval via semantic search (Reimers and Gurevych, 2020).

To alleviate this issue, Reimers and Gurevych (2019) developed SentenceBERT (SBERT), which is a modification of the BERT network using Siamese and Triplet networks that can derive semantically meaningful sentence embedding.

The Siamese network architecture enables input sentences to be fixed-sized vectors. Thus, we use SBERT to find a similar weather conditions on 12 January 1914 (query) from all the corpora available (general weather report commentary on daily weather chart 1996-2021). Figure B5 explains all steps to find similar weather conditions through a semantic search based on STS between the old and the modern commentaries. We define the corpora as a collection of a commentaries, which may contain one or more sentences explaining the weather conditions in a non-uniform sequence. SBERT embeds each sentence on both query and corpus with pre-trained models, specifically to handle the Japanese language. The result of the sentence embedding is vectors with a length of 768 values, specific to each sentence, representing the sentence in the vector space (Reimers and Gurevych, 2019).

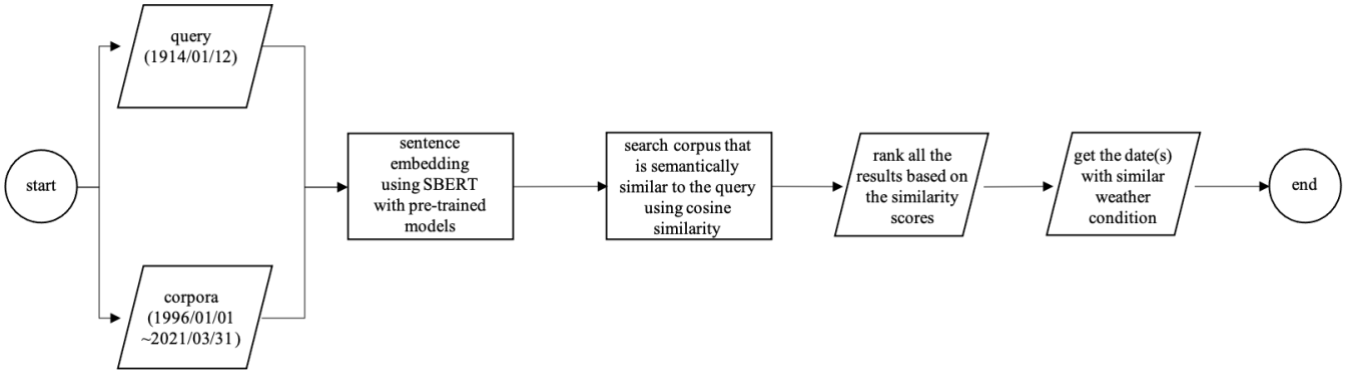

Figure B5. The flowchart for finding the date with a similar weather report commentary to the day of eruption using SBERT.

We employed pre-trained models available for the Japanese language from the Hugging Face model hub (Hugging Face, 2022). However, sentence embedding resources for the Japanese language are limited, and we found only one appropriate pre-trained model exclusively developed for Japanese sentences, *sbert-base-ja* (Abe, 2021). This pre-trained model is from Colorful Scoop, a non-profit entity developing a conversational AI (Colorful Scoop, 2022). This company produced its own BERT Japanese model, which is trained using the Japanese Wikipedia corpus and released in 2021 under the CC-BY-SA 3.0 licence. The *sbert-base-ja* pre-trained model is an extension of their original model and is trained using the Japanese translation of the Stanford Natural Language Inference (JSNLI) dataset released by Kyoto University under CC-BY-SA 4.0 licence (Yoshikushi et al., 2020), with 535,000 sentence pairs, utilising AdamW optimiser with a $2x10^{-5}$ learning rate (Abe, 2021). Once we encode both queries and corpora into the vector space, we conduct a semantic search to find the most similar commentary between the query and corpora. The benefit of using semantic search is that we can find synonymous sentences, although constructed using completely different words and order, as the search process focuses on understanding the query's content. Specifically, we performed a symmetric semantic search because both the query and corpus have similar lengths and numbers of sentences (Reimers and Gurevych, 2019). We used cosine similarity to compute the similarity scores between the query and all corpora.

Cosine similarity is a popular similarity metric used to identify a pair of sentences with an overlapping meanings, as these sentences are likely to be located next to each other in the vector space (Cer et al., 2017; Reimers and Gurevych, 2019; Arsov et al., 2019).

$$\mathrm{sim}_{\mathrm{v}}(q, c) = \frac{\mathrm{v}(q) \cdot \mathrm{v}(c)}{\|\mathrm{v}(q)\|_2 \|\mathrm{v}(c)\|_2} \quad (5)$$

Given a pair of sentence vectors $\mathrm{v}(q)$ and $\mathrm{v}(c)$, cosine similarity $\mathrm{sim}_{\mathrm{v}}$ is computed by the dot product and the magnitude between two vectors, where q and c are the components of vector $\mathrm{v}(q)$ and vector $\mathrm{v}(c)$, respectively. Here, q is each sentence in the queries, which is the feature we want to find, and c is each sentence in all the commentaries collected from 1996 to 2021.

Table B2. The top 10 weather similarities scores of the selected dates.

Date	STS Score
5 March 1997	**0.9635**
24 February 2006	0.9575
2 February 2011	0.9551
11 December 1996	0.9532
16 March 2001	0.9514
30 March 2009	0.9508
28 January 2009	0.9507
29 December 1996	0.9503
19 January 2019	0.9497
14 January 2005	0.9496

Table B3: The top result of the semantic search process with its weather description from the commentary.

Date	STS Score	Commentary (ja)	Commentary (en)
1997/03/05	0.963	*全国的に平年より5~10℃高い。日本付近は移動性高気圧に覆われるが、大陸から気圧の谷が進んでくる。北海道で曇りの他は似中晴れ。夜になると日本海側は曇り。山陰や九州北部では雨。*	*5~10℃ above normal nationwide.* ***A mobile high-pressure system will cover the area around Japan****, but a trough of pressure will move in from the continent.* ***Mostly cloudy in Hokkaido and sunny throughout****. Cloudy over the Sea of Japan at night. Rain in the San-in region and northern Kyushu.*

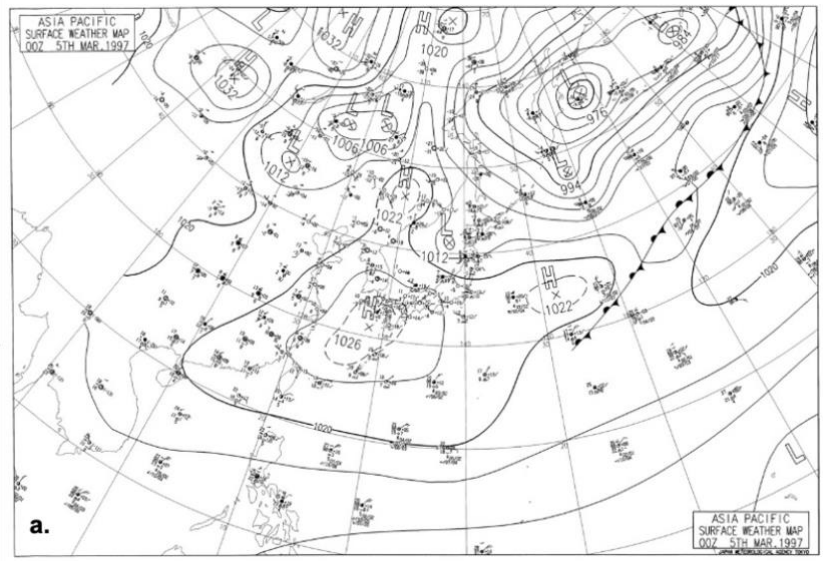

Figure B6. Surface weather chart for Asia Pacific region at 00 UTC 5 March 1997. Weather chart image is obtained from the JMA (Database of Weather Charts for Hundred Years, 2022; Daily Weather Chart, 2022).

The results of the comparison are between {0} for the most dissimilar sentences, and {1} if a pair of sentences is very similar (Singhal, 2001). The last step is to find similar weather conditions by ranking all corpora based on their similarity scores with the query. In brief, we selected only the top highest result from the top 10 results obtained from the search process, as shown in Table B2. Table B3 describes the general commentary on the top results of the semantic search. The commentary in English is a direct translation using DeepL translation software (DeepL Translator, 2022), with sentences in bold indicating weather conditions similar to the Taisho eruption.

B.2.3 Weather condition on the selected date

The date with the highest STS scores (5 March 1997) agreed well with the weather features mentioned in the chronicles. The weather on selected date was generally clear and sunny because of the high-pressure covering Japan's main islands. With the exception of some rain that the chronicles did not mention. This difference indicate that we may not observe the exactly similar weather completely. This slight difference may affect the ashfall distribution produced by the simulation slightly. Figure B6 depicts the weather chart for the chosen date, illustrating more apparent features analogous to the weather chart published during the eruption. Both the chosen date and the eruption date exhibit the same weather characteristics, as high-pressure covering entire Japan regions, added with an influence of a low-pressure centre in the north. On the selected date, the high-pressure centre moved from the south and then covered Japan at night. The weather charts presented in Fig. B6 further substantiate the continuous format transition of surface weather analysis in Japan. The general weather report

commentary, accompanied by the establishment of a daily weather chart, is proven to be critical information that clarifies the weather conditions on the respective date.

Another feature, not mentioned in the commentary was the wind conditions during the selected dates. The chronicles briefly revealed that the wind was weak, making it possible to evacuate using boats from the island to escape the eruption (Omori, 1914; Kitagawa, 2015). To further analyse the weather similarities between the selected date and 12 January 1914, we drew the condition of the wind using a wind rose graph as depicted in Fig. B7.

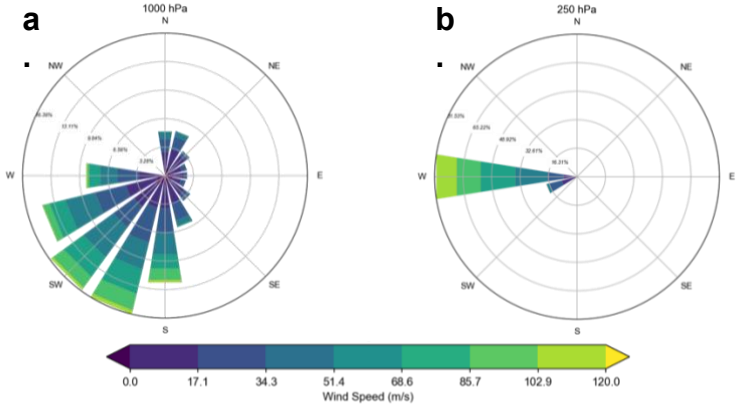

Figure B7. The wind rose diagrams show the six-hourly wind direction on 5 March to 10 March 1997, corresponding to which from the winds blow at (a) 1000 hPa altitude (~100 m asl.), and (b) 250 hPa altitude (~10 km asl.).

The graph consists of winds observations for every 6 h from the start of the simulation (00 UTC on the selected date) until the simulation process finished (00 UTC four days after the eruption start). We chose the winds observations both at the 1000 hPa pressure level (equivalent to the surface pressure) and 250 hPa pressure level (equivalent to the location of the westerlies) based on the findings explained in Sect. 2. The surface winds characteristics differed in terms of directions but had a comparable velocity between the two selected dates. The winds surface winds during the eruption day are akin to the selected date, regarding the dominant southwesterly winds portrayed in Fig. B7. The upper winds in March 1997 had a stronger velocity but mostly came from the west, due to the westerlies cycle.

Author contributions

HR performed most of the work to produce the dataset by performing the data processing and simulations, analysing the results, and writing this manuscript. In addition, HT conceptualised the project and supervised both the simulations and the results analysis. MI produced the Taisho eruption data used as the eruption source parameters used in the model to generate the dataset. HLT is the creator of the PUFF model, provided the original FORTRAN codes of the model and the default values of the parameters used in the simulation. TT verified the weather similarity process by incorporating the general

weather report commentary inside the weather chart. SR assisted in developing a semantic search methodology to find the semantic similarities through the commentary.

Competing Interest

The authors declare that they have no conflict of interest.

Acknowledgements

We acknowledge the works of the Sakurajima Volcano Research Center (SVRC), Disaster Prevention Research Institute, Kyoto University in Kagoshima, Japan, which provided the Taisho eruption data used in this study. In addition, we thank the JMA for supplying the JRA-55 Reanalysis data from 1958 to 2020. The JRA-55 data were obtained from the archive of the Center for Computational Sciences (CCS), University of Tsukuba, Ibaraki, Japan. Furthermore, the authors are grateful for the help from Si Ha, Ryo Hirako, and Toraemon Matsumoto, who assisted in the map digitalisation process of the original ash dispersal map and the translation process for the old weather charts. HR acknowledges fellowship and financial support from the Tokio Marine Kagami Memorial Foundation for this work. We would like to thank Editage (www.editage.com) for English language editing.

References

Abe, N.: Sentence BERT Base Japanese Model, Python, Colorful Scoop, 2021.

Agirre, E., Cer, D., Diab, M., and Gonzalez-Agirre, A.: SemEval-2012 Task 6: A pilot on semantic textual similarity, in: Proceedings of the Sixth International Workshop on Semantic Evaluation (SemEval 2012), SEM 2012: The First Joint Conference on Lexical and Computational Semantics, Montréal, Canada, 385–393, 2012.

Arsov, N., Dukovski, M., Evkoski, B., and Cvetkovski, S.: A Measure of Similarity in Textual Data Using Spearman's Rank Correlation Coefficient, ArXiv [eprint], arXiv:1911.11750, 2019.

Ayris, P. M. and Delmelle, P.: The immediate environmental effects of tephra emission, Bull. Volcanol., 74, 1905–1936, https://doi.org/10.1007/s00445-012-0654-5, 2012.

Barsotti, S., Andronico, D., Neri, A., Del Carlo, P., Baxter, P. J., Aspinall, W. P., and Hincks, T.: Quantitative assessment of volcanic ash hazards for health and infrastructure at Mt. Etna (Italy) by numerical simulation, J. Volcanol. Geotherm. Res., 192, 85–96, https://doi.org/10.1016/j.jvolgeores.2010.02.011, 2010.

Barsotti, S., Di Rienzo, D. I., Thordarson, T., Björnsson, B. B., and Karlsdóttir, S.: Assessing impact to infrastructures due to tephra fallout from Öræfajökull volcano (Iceland) by using a scenario-based approach and a numerical model, Front. Earth Sci., 6, 196, https://doi.org/10.3389/feart.2018.00196, 2018.

Biass, S., Scaini, C., Bonadonna, C., Folch, A., Smith, K., and Höskuldsson, A.: A multi-scale risk assessment for tephra fallout and airborne concentration from multiple Icelandic volcanoes – Part 1: Hazard assessment, Nat. Hazards Earth Syst. Sci., 14, 2265–2287, https://doi.org/10.5194/nhess-14-2265-2014, 2014.

Biass, S., Bonadonna, C., di Traglia, F., Pistolesi, M., Rosi, M., and Lestuzzi, P.: Probabilistic evaluation of the physical impact of future tephra fallout events for the Island of Vulcano, Italy, Bull. Volcanol, 78, 37, https://doi.org/10.1007/s00445-016-1028-1, 2016.

Biass, S., Todde, A., Cioni, R., Pistolesi, M., Geshi, N., and Bonadonna, C.: Potential impacts of tephra fallout from a large-scale explosive eruption at Sakurajima volcano, Japan, Bull. Volcanol., 79, https://doi.org/10.1007/s00445-017-1153-5, 2017.

Bonadonna, C.: Probabilistic modelling of tephra dispersion, in: Statistics in Volcanology, Special Publications of IAVCEI, 1, edited by: Mader, H. M., Coles, S. G., Connor, C. B., and Connor, L. J., The Geological Society of London on behalf of The International Association of Volcanology and Chemistry of the Earth's Interior, 243–259, https://doi.org/10.1144/IAVCEI001.19, 2006.

Bonadonna, C., Ernst, G. G. J., and Sparks, R. S. J.: Thickness variations and volume estimates of tephra fall deposits: The importance of particle Reynolds number, J. Volcanol. Geotherm. Res., 81, 173–187, https://doi.org/10.1016/S0377-0273(98)00007-9, 1998.

Bonadonna, C., Folch, A., Loughlin, S., and Puempel, H.: Future developments in modelling and monitoring of volcanic ash clouds: Outcomes from the first IAVCEI-WMO workshop on Ash Dispersal Forecast and Civil Aviation, Bull. Volcanol., 74, 1–10, https://doi.org/10.1007/s00445-011-0508-6, 2012.

Bonadonna, C., Biass, S., Menoni, S., and Gregg, C. E.: Assessment of risk associated with tephra-related hazards, in: Forecasting and Planning for Volcanic Hazards, Risks, and Disasters, 2, edited by: Schroeder, J. F., volume edited by, Papale, P., Elsevier, 329–378, https://doi.org/10.1016/B978-0-12-818082-2.00008-1, 2021.

Bursik, M., Jones, M., Carn, S., Dean, K., Patra, A., Pavolonis, M., Pitman, E. B., Singh, T., Singla, P., Webley, P., Bjornsson, H., and Ripepe, M.: Estimation and propagation of volcanic source parameter uncertainty in an ash transport and dispersal model: Application to the Eyjafjallajokull plume of 14–16 April 2010, Bull. Volcanol., 74, 2321–2338, https://doi.org/10.1007/s00445-012-0665-2, 2012.

Central Disaster Management Council, Executive Committee for Disaster Prevention: Impacts of Ashfall and Countermeasures in the Tokyo Metropolitan Area: Mt. Fuji Eruption Case (in Japanese), Working Group on Ashfall Countermeasures for Large-Scale Eruptions, Cabinet Office, Government of Japan, 2020.

Cer, D., Diab, M., Agirre, E., Lopez-Gazpio, I., and Specia, L.: SemEval-2017 Task 1: Semantic textual similarity – Multilingual and cross-lingual focused evaluation, in: Proceedings of the 11th International Workshop on Semantic Evaluation (SemEval-2017), 11th International Workshop on Semantic Evaluation (SemEval-2017), Vancouver, Canada, 1–14, https://doi.org/10.18653/v1/S17-2001, 2017.

Colorful Scoop: https://colorfulscoop.com/, last access: 27 January 2022.

Daily weather chart: https://www.data.jma.go.jp/fcd/yoho/hibiten/, last access: 3 January 2022.

Damby, D. E., Horwell, C. J., Baxter, P. J., Delmelle, P., Donaldson, K., Dunster, C., Fubini, B., Murphy, F. A., Nattrass, C., Sweeney, S., Tetley, T. D., and Tomatis, M.: The respiratory health hazard of tephra from the 2010 Centennial eruption of

Merapi with implications for occupational mining of deposits, J. Volcanol. Geotherm. Res., 261, 376–387, https://doi.org/10.1016/j.jvolgeores.2012.09.001, 2013.

Database of weather charts for hundred years: http://agora.ex.nii.ac.jp/digital-typhoon/weather-chart/, last access: 3 January 2022.

Environmental Systems Research Institute (ESRI): ArcGIS Pro 2.7, 2017.

Environmental Systems Research Institute (ESRI): Human geography base [basemap], https://www.arcgis.com/home/item.html?id=2afe5b807fa74006be6363fd243ffb30, 2022.

Deep, L. translator: https://www.deepl.com/translator/, last access: 27 January 2022.

Devlin, J., Chang, M.-W., Lee, K., and Toutanova, K.: BERT: Pretraining of Deep Bidirectional Transformers for Language Understanding, ArXiv [eprint], arXiv:1810.04805, 2019.

Eliasson, J., Yoshitani, J., Weber, K., Yasuda, N., Iguchi, M., and Vogel, A.: Airborne measurement in the ash plume from mount Sakurajima: Analysis of gravitational effects on dispersion and fallout, Int. J. Atmos. Sci., 2014, 1–16, https://doi.org/10.1155/2014/372135, 2014.

Fero, J., Carey, S. N., and Merrill, J. T.: Simulation of the 1980 eruption of Mount St. Helens using the ash-tracking model PUFF, J. Volcanol. Geotherm. Res., 175, 355–366, https://doi.org/10.1016/j.jvolgeores.2008.03.029, 2008.

Fero, J., Carey, S. N., and Merrill, J. T.: Simulating the dispersal of tephra from the 1991 Pinatubo eruption: Implications for the formation of widespread ash layers, J. Volcanol. Geotherm. Res., 186, 120–131, https://doi.org/10.1016/j.jvolgeores.2009.03.011, 2009.

Folch, A.: A review of tephra transport and dispersal models: Evolution, current status, and future perspectives, J. Volcanol. Geotherm. Res., 235–236, 96–115, https://doi.org/10.1016/j.jvolgeores.2012.05.020, 2012.

Folch, A., Costa, A., Durant, A., and Macedonio, G.: A model for wet aggregation of ash particles in volcanic plumes and clouds: 2. Model application, J. Geophys. Res., 115, B09202, https://doi.org/10.1029/2009JB007176, 2010.

Folch, A., Costa, A., and Basart, S.: Validation of the FALL3D ash dispersion model using observations of the 2010 Eyjafjallajökull volcanic ash clouds, Atmos. Environ., 48, 165–183, https://doi.org/10.1016/j.atmosenv.2011.06.072, 2012.

Hampton, S. J., Cole, J. W., Wilson, G., Wilson, T. M., and Broom, S.: Volcanic ashfall accumulation and loading on gutters and pitched roofs from laboratory empirical experiments: Implications for risk assessment, J. Volcanol. Geotherm. Res., 304, 237–252, https://doi.org/10.1016/j.jvolgeores.2015.08.012, 2015.

Hattori, Y., Suto, H., Toshida, K., and Hirakuchi, H.: Development of Estimation Method for Tephra Transport and Dispersal Characteristics with Numerical Simulation Technique (part 1) – Meteorological Effects on Ash Fallout with Shinmoe-dake Eruption (in Japanese), Central Research Institute of Electric Power Industry (CRIEPI), Japan, 2013.

Hattori, Y., Suto, H., Toshida, K., and Hirakuchi, H.: Development of Estimation Method for Tephra Transport and Dispersal Characteristics with Numerical Simulation Technique (part 2) – A Method of Selecting Meteorological Conditions and the Effects on Ash Deposition and Concentration in Air for Kanto-Area (in Japanese), Central Research Institute of Electric Power Industry (CRIEPI), Japan, 2016.

Hickey, J., Gottsmann, J., Nakamichi, H., and Iguchi, M.: Thermomechanical controls on magma supply and volcanic deformation: Application to Aira caldera, Japan, Sci Rep, Sci. Rep., 6, 32691, https://doi.org/10.1038/srep32691, 2016.

Hoyer, S. and Hamman, J. J.: xarray: N-D labeled Arrays and Datasets in Python, J. Open Res. Softw., 5, https://doi.org/10.5334/jors.148, 2017.

Face, H.: https://huggingface.co/, last access: 27 January 2022.

Iguchi, M.: Sakurajima Taisho Eruption, 100th Anniversary of the Disaster Prevention in Sakurajima, Kyoto University, Kyoto, Japan, 2014.

Iguchi, M.: Method for real-time evaluation of discharge rate of volcanic ash – Case study on intermittent eruptions at the Sakurajima volcano, Japan, J. Disaster Res., 11, 4–14, https://doi.org/10.20965/jdr.2016.p0004, 2016.

Iguchi, M., Nakamichi, H., and Tameguri, T.: Integrated study on forecasting volcanic hazards of Sakurajima volcano, Japan, J. Disaster Res., 15, 174–186, https://doi.org/10.20965/jdr.2020.p0174, 2020.

Japan's Daily Weather Chart, Japan Meteorological Agency: https://www.data.jma.go.jp/fcd/yoho/hibiten/, last access: 3 January 2022.

Jenkins, S. F., Spence, R. J. S., Fonseca, J. F. B. D., Solidum, R. U., and Wilson, T. M.: Volcanic risk assessment: Quantifying physical vulnerability in the built environment, J. Volcanol. Geotherm. Res., 276, 105–120, https://doi.org/10.1016/j.jvolgeores.2014.03.002, 2014.

Jenkins, S. F., Wilson, T. M., Magill, C., Miller, V., Stewart, C., Blong, R., Marzocchi, W., Boulton, M., Bonadonna, C., and Costa, A.: Volcanic ash fall hazard and risk, in: Global Volcanic Hazards and Risk, edited by: Loughlin, S. C., Sparks, S., Brown, S. K., Jenkins, S. F., and Vye-Brown, C., Cambridge University Press, Cambridge, 173–222, https://doi.org/10.1017/CBO9781316276273.005, 2015.

Jenkins, S. F., Magill, C. R., and Blong, R. J.: Evaluating relative tephra fall hazard and risk in the Asia-Pacific region, Geosphere, 14, 492–509, https://doi.org/10.1130/GES01549.1, 2018.

Jurafsky, D. and James, M. H.: Speech and Language Processing: An Introduction to Natural Language Processing, Computational Linguistics, and Speech Recognition, Prentice Hall, Upper Saddle River, NJ, 2000.

Kagoshima City, Crisis Management Division: Sakurajima Volcano Hazard Map, Kagoshima Municipal Government, Kagoshima, Japan, 2010.

Kitagawa, K.: Living with an active volcano: Informal and community learning for preparedness in south of Japan, in: Observing the Volcano World, edited by: Fearnley, C. J., Bird, D. K., Haynes, K., McGuire, W. J., and Jolly, G., Springer International Publishing, Cham, 677–689, https://doi.org/10.1007/11157_2015_12, 2015.

Kobayashi, S., Ota, Y., Harada, Y., Ebita, A., Moriya, M., Onoda, H., Onogi, K., Kamahori, H., Kobayashi, C., Endo, H., Miyaoka, K., and Takahashi, K.: The JRA-55 reanalysis: General specifications and basic characteristics, J. Meteorol. Soc. Jpn, 93, 5–48, https://doi.org/10.2151/jmsj.2015-001, 2015.

Kobayashi, T.: Geology of Sakurajima volcano: A review, Bull. Volcanol. Soc. Jpn, 27, 277–292, 1982.

Koto, B.: The great eruption of Sakura-Jima, J. Coll. Sci. Imperial Univ. Tokyo, 38, 1–237, 1916.

Kratzmann, D. J., Carey, S. N., Fero, J., Scasso, R. A., and Naranjo, J.-A.: Simulations of tephra dispersal from the 1991 explosive eruptions of Hudson volcano, Chile, Journal of Volcanology and Geothermal Research, 190, 337–352, https://doi.org/10.1016/j.jvolgeores.2009.11.021, 2010.

Kyushu Regional Development Bureau and Osumi Office of the Rivers and National Highways: Sakurajima volcano wide area disaster prevention map (in Japanese), Minist. Land Infrastruct. Transp. Tourism Sakurajima, Kagoshima, Japan, 2017.

Lin, J., Brunner, D., Gerbig, C., Stohl, A., Luhar, A., and Webley, P.: Lagrangian modeling of the atmosphere: An introduction, in: Lagrangian Modeling of the Atmosphere, American Geophysical Union, Washington, DC, USA, 1–15, 2012.

Macedonio, G., Costa, A., Scollo, S., and Neri, A.: Effects of eruption source parameter variation and meteorological dataset on tephra fallout hazard assessment: Example from Vesuvius (Italy), J. Appl. Volcanol., 5, 5, https://doi.org/10.1186/s13617-016-0045-2, 2016.

Madankan, R., Pouget, S., Singla, P., Bursik, M., Dehn, J., Jones, M., Patra, A., Pavolonis, M., Pitman, E. B., Singh, T., and Webley, P.: Computation of probabilistic hazard maps and source parameter estimation for volcanic ash transport and dispersion, J. Comput. Phys., 271, 39–59, https://doi.org/10.1016/j.jcp.2013.11.032, 2014.

Maeda, S., Hirahara, S., Hagiya, S., Murai, H., and Oikawa, Y., 05 March 2012: Forecasting Changes in Seasonal Progress in Future Climate (based on the changes of Westerly Wind) (in Japanese): http://wind.gp.tohoku.ac.jp/yamase/reports/meeting5.html, Climate Information Division, Global Environment and Ocean Department, Japan Meteorological Agency.

Mastin, L. G., Guffanti, M., Servranckx, R., Webley, P., Barsotti, S., Dean, K., Durant, A., Ewert, J. W., Neri, A., Rose, W. I., Schneider, D., Siebert, L., Stunder, B., Swanson, G., Tupper, A., Volentik, A., and Waythomas, C. F.: A multidisciplinary effort to assign realistic source parameters to models of volcanic ash-cloud transport and dispersion during eruptions, J. Volcanol. Geotherm. Res., 186, 10–21, https://doi.org/10.1016/j.jvolgeores.2009.01.008, 2009.

Mita, K., Ishimine, Y., Iwamatsu, A., Kamikozuru, H., Koga, M., Takeda, N., Nakamura, T., Matsumoto, S., Iguchi, M., Baba, M., Yamaguchi, K., Shimokawa, E., and Maki, M.: Tentative Reports on the Traffic Countermeasures for a Large-Scale Eruption of Sakurajima Volcano. Case Study: Ash Deposit on Kagoshima City (in Japanese), Earthquake and Volcanic Disaster Prevention Center, Kagoshima University, 2018.

Miyaji, N., Kan'no, A., Kanamaru, T., and Mannen, K.: High-resolution reconstruction of the Hoei eruption (AD 1707) of Fuji volcano, Japan, J. Volcanol. Geotherm. Res., 207, 113–129, https://doi.org/10.1016/j.jvolgeores.2011.06.013, 2011.

Morton, B. R., Taylor, S. G., and Turner, J. S.: Turbulent gravitational convection from maintained and instantaneous sources: Proceedings of the R. Soc. Lond. A Mat., 234, 1–23, https://doi.org/10.1098/rspa.1956.0011, 1956.

Newhall, C. G. and Self, S.: The volcanic explosivity index (VEI) an estimate of explosive magnitude for historical volcanism, J. Geophys. Res., 87, 1231, https://doi.org/10.1029/JC087iC02p01231, 1982.

Nishimura, T.: Source mechanisms of volcanic explosion earthquakes: Single force and implosive sources, J. Volcanol. Geotherm. Res., 86, 97–106, https://doi.org/10.1016/S0377-0273(98)00088-2, 1998.

Omori, F.: The Sakura-Jima eruption and earthquakes, Bulletin of the Imperial Earthquake Investigation Committee, University of Tokyo, 8, 1–630, 1914.

Peng, J. and Peterson, R.: Attracting structures in volcanic ash transport, Atmos. Environ., 48, 230–239, https://doi.org/10.1016/j.atmosenv.2011.05.053, 2012.

Peterson, R. and Dean, K.: Analysis and Optimization of a Lagrangian Volcanic Ash Particle Tracking Model called Puff, AGU Fall Meet. Admin., 2002.

Poulidis, A. P. and Takemi, T.: A 1998–2013 climatology of Kyushu, Japan: Seasonal variations of stability and rainfall, Int. J. Climatol., 37, 1843–1858, https://doi.org/10.1002/joc.4817, 2017.

Poulidis, A. P., Takemi, T., Iguchi, M., and Renfrew, I. A.: Orographic effects on the transport and deposition of volcanic ash: A case study of Mount Sakurajima, Japan, J. Geophys. Res. Atmos., 122, 9332–9350, https://doi.org/10.1002/2017JD026595, 2017.

Poulidis, A. P., Takemi, T., Shimizu, A., Iguchi, M., and Jenkins, S. F.: Statistical analysis of dispersal and deposition patterns of volcanic emissions from MT. Sakurajima, Japan, Atmos. Environ., 179, 305–320, https://doi.org/10.1016/j.atmosenv.2018.02.021, 2018.

Rahadianto, H. and Tatano, H.: 62 Years Simulated Sakurajima Taisho Eruption Ashfall Deposit Data (1958-2019), Disaster Prevention Research Institute, Kyoto University, Japan [dataset], https://doi.org/10.17603/ds2-vw5f-t920, 2020.

Rathje, E. M., Dawson, C., Padgett, J. E., Pinelli, J.-P., Stanzione, D., Adair, A., Arduino, P., Brandenberg, S. J., Cockerill, T., Dey, C., Esteva, M., Haan, F. L., Hanlon, M., Kareem, A., Lowes, L., Mock, S., and Mosqueda, G.: DesignSafe: New cyberinfrastructure for natural hazards engineering, Nat. Hazards Rev., 18, 06017001, https://doi.org/10.1061/(ASCE)NH.1527-6996.0000246, 2017.

Reimers, N. and Gurevych, I.: Sentence-BERT: Sentence Embeddings Using Siamese BERT-Networks, ArXiv [eprint], arXiv:1908.10084, 2019.

Reimers, N. and Gurevych, I.: Making Monolingual Sentence Embeddings Multilingual Using Knowledge Distillation, ArXiv [eprint], arXiv:2004.09813, 2020.

Scollo, S., Prestifilippo, M., Coltelli, M., Peterson, R. A., and Spata, G.: A statistical approach to evaluate the tephra deposit and ash concentration from PUFF model forecasts, J. Volcanol. Geotherm. Res., 200, 129–142, https://doi.org/10.1016/j.jvolgeores.2010.12.004, 2011.

Searcy, C., Dean, K., and Stringer, W.: PUFF: A high-resolution volcanic ash tracking model, J. Volcanol. Geotherm. Res., 80, 1–16, https://doi.org/10.1016/S0377-0273(97)00037-1, 1998.

Selva, J., Costa, A., De Natale, G., Di Vito, M. A., Isaia, R., and Macedonio, G.: Sensitivity test and ensemble hazard assessment for tephra fallout at Campi Flegrei, Italy, J. Volcanol. Geotherm. Res., 351, 1–28, https://doi.org/10.1016/j.jvolgeores.2017.11.024, 2018.

Shimbori, T., Aikawa, Y., Fukui, K., Hashimoto, A., Seino, N., and Yamasato, H.: Quantitative tephra fall prediction with the JMA mesoscale tracer transport model for volcanic ash: A case study of the eruption at Asama volcano in 2009 (in Japanese), Pap. Meteorol. Geophys., 61, 13–29, https://doi.org/10.2467/mripapers.61.13, 2009.

Singhal, A.: Modern Information Retrieval: A Brief Overview, 9, 2001.

Takebayashi, M., Onishi, M., and Iguchi, M.: Large volcanic eruptions and their influence on air transport: The case of Japan, J. Air Transp. Manag., 97, 102136, https://doi.org/10.1016/j.jairtraman.2021.102136, 2021.

Tanaka, H. L.: Development of A prediction scheme for volcanic ash fall from redoubt volcano, Alaska, in: Proceedings of the First International Symposium on Volcanic Ash and Aviation Safety, First International Symposium on Volcanic Ash and Aviation Safety, 283–291, https://doi.org/10.3133/b2047, 1994.

Tanaka, H. L. and Iguchi, M.: Numerical simulations of volcanic ash plume dispersal for Sakura-Jima using real-time emission rate estimation, J. Disaster Res., 14, 160–172, https://doi.org/10.20965/jdr.2019.p0160, 2019.

Tanaka, H. L. and Yamamoto, K.: Numerical simulation of volcanic plume dispersal from usu volcano in Japan on 31 March 2000 using PUFF model, Earth Planets Space, 54, 743–752, https://doi.org/10.1186/BF03351727, 2002.

Tanaka, H. L., Iguchi, M., and Nakada, S.: Numerical simulations of volcanic ash plume dispersal from Kelud volcano in Indonesia on February 13, 2014, J. Disaster Res., 11, 31–42, https://doi.org/10.20965/jdr.2016.p0031, 2016.

Tilling, R. I., Topinka, L. J., Swanson, D. A., and Survey (U.S.), G.: Eruptions of Mount St. Helens: Past, Present, and Future, US Department of the Interior, Geological Survey, 1990.

Todde, A., Cioni, R., Pistolesi, M., Geshi, N., and Bonadonna, C.: The 1914 Taisho eruption of Sakurajima volcano: Stratigraphy and dynamics of the largest explosive event in Japan during the twentieth century, Bull. Volcanol., 79, 72, https://doi.org/10.1007/s00445-017-1154-4, 2017.

Tsukui, M.: Ash-fall distribution of 1779 an'ei eruption, Sakurajima volcano: Revealed by historical documents (in Japanese), Bull. Volcanological Soc. Jpn, 56, 89–94, https://doi.org/10.18940/kazan.56.2-3_89, 2011.

Unidata: NetCDF, UCAR/Unidata, https://doi.org/10.5065/D6H70CW6, 2021.

Wallace, J. M. and Hobbs, P. V.: Atmospheric Science: An Introductory Survey, 2nd ed, Academic Press, Amsterdam, Paris, 2006.

Webley, P. and Mastin, L.: Improved prediction and tracking of volcanic ash clouds, J. Volcanol. Geotherm. Res., 186, 1–9, https://doi.org/10.1016/j.jvolgeores.2008.10.022, 2009.

Wilson, T. M., Stewart, C., Sword-Daniels, V., Leonard, G. S., Johnston, D. M., Cole, J. W., Wardman, J., Wilson, G., and Barnard, S. T.: Volcanic ash impacts on critical infrastructure, Phys. Chem. Earth Parts A B C, 45–46, 5–23, https://doi.org/10.1016/j.pce.2011.06.006, 2012.

Yamasato, H., Funasaki, J., and Takagi, Y.: The Japan Meteorological Agency's Volcanic Disaster Mitigation Initiatives, National Research Institute for Earth Science and Disaster Prevention, Japan, 2013.

Yasui, M., Takahashi, M., Ishihara, K., and Miki, D.: Records on the 1914–1915 eruption of Sakurajima volcano, Japan (in Japanese), Bull. Volcanological Soc. Jpn, 41, 75–107, 2006.

Yasui, M., Takahashi, M., Ishihara, K., and Miki, D.: Eruptive Style and Its Temporal Variation through the 1914–1915 Eruption of Sakurajima Volcano, 52, Southern Kyushu, Japan (in Japanese), Bulletin of The Volcanological Society of Japan, 161–186, https://doi.org/10.18940/kazan.52.3_161, 2007.

Yoshikushi, T., Kawahara, D., and Kurohara, S.: Multilingualization of a Natural Language Inference Dataset Using Machine Translation, Kyoto University, 2020.

Zuccaro, G., Leone, M. F., Del Cogliano, D., and Sgroi, A.: Economic impact of explosive volcanic eruptions: A simulation-based assessment model applied to Campania region volcanoes, J. Volcanol. Geotherm. Res., 266, 1–15, https://doi.org/10.1016/j.jvolgeores.2013.09.002, 2013.